

Space Weather®

<u>_</u>

RESEARCH ARTICLE

10.1029/2022SW003216

Key Points:

- The sensitivity of a whole atmospheric model, Whole Atmosphere Community Climate Model with thermosphere and ionosphere eXtension, to forcing uncertainties is evaluated using ensemble simulation
- Impact of high-latitude forcing uncertainty is large during storm-time, and impact of the lower-atmospheric forcings are always significant
- The response of the upper atmosphere to these uncertainties cannot be superposed linearly, implying the non-linearities in the T-I system

Supporting Information:

Supporting Information may be found in the online version of this article.

Correspondence to:

C.-T. Hsu, chihting@ucar.edu

Citation:

Hsu, C.-T., & Pedatella, N. M. (2023). Effects of forcing uncertainties on the thermospheric and ionospheric states during geomagnetic storm and quiet periods. *Space Weather*, *21*, e2022SW003216. https://doi.org/10.1029/2022SW003216

Received 12 JUL 2022 Accepted 22 MAR 2023

Author Contributions:

Conceptualization: C.-T. Hsu Formal analysis: C.-T. Hsu Funding acquisition: N. M. Pedatella Methodology: C.-T. Hsu

Project Administration: N. M. Pedatella

Software: C.-T. Hsu
Supervision: N. M. Pedatella
Validation: C.-T. Hsu
Visualization: C.-T. Hsu
Writing – original draft: C.-T. Hsu

© 2023. The Authors.

This is an open access article under the terms of the Creative Commons Attribution-NonCommercial-NoDerivs License, which permits use and distribution in any medium, provided the original work is properly cited, the use is non-commercial and no modifications or adaptations are made.

Effects of Forcing Uncertainties on the Thermospheric and Ionospheric States During Geomagnetic Storm and Quiet Periods

C.-T. Hsu¹ and N. M. Pedatella¹

¹High Altitude Observatory, National Center for Atmospheric Research, Boulder, CO, USA

Abstract Upper-atmospheric weather prediction is subject to various types of forcing uncertainties. Understanding the sensitivity of the thermosphere and ionosphere to forcing uncertainties under different geomagnetic conditions is critical for space weather predictions. Ensemble simulations of a whole atmospheric model, the National Center for Atmospheric Research Whole Atmosphere Community Climate Model with thermosphere and ionosphere eXtension (WACCM-X), with various kinds of forcing perturbation is used to evaluate the upper atmosphere's response to the uncertainties of different forcings. Two kinds of forcing uncertainties are addressed: the lower atmospheric wave and tide forcing uncertainties and high-latitude electric potential uncertainty. These uncertainties are estimated in different ways and applied to generate forcing perturbations in the WACCM-X. WACCM-X can simulate the upper atmosphere's response to the uncertainties of the lower atmospheric wave and tide forcings related to different lower atmospheric conditions. High-latitude electric potential uncertainty is estimated based on the SuperMag and SuperDARN data through the Assimilative Mapping of Geospace Observations, which is applied to generate the forcing perturbation of high-latitude electric potential in the WACCM-X. The results show that the impact of high-latitude electric potential uncertainty is significant globally during the 2013 St. Patrick's Day storm. The lower atmospheric wave and tide forcing uncertainties result in a global impact on the upper atmosphere in the model. The sensitivity of the upper atmosphere to both uncertainties is approximately the combination of the two individually, though the combined effects are not a linear sum, indicating non-linearities in the ionosphere and thermosphere response to forcing uncertainties.

Plain Language Summary The upper-atmospheric weather is driven by several forcing mechanisms. Since the forcing is difficult to quantify, there is uncertainty in the forcing that will lead to uncertainties in the thermosphere and ionosphere. Understanding the upper atmosphere's sensitivity to the forcing uncertainties is important. This study focuses on the uncertainties of energy input from the magnetosphere (represented by the high-latitude electric potential) and lower-atmospheric wave variability. A whole atmosphere model, the National Center for Atmospheric Research Whole Atmosphere Community Climate Model with thermosphere and ionosphere eXtension (WACCM-X), is used to evaluate the upper atmosphere's response to these two types of forcing uncertainties. The lower-atmospheric wave and tide forcings can be generated through atmospheric dynamics in the WACCM-X. The high-latitude electric potential can be estimated based on the SuperMag and SuperDARN data. A set of WACCM-X simulations is launched during the 2013 St. Patrick's Day storm, and forcings in each simulation are perturbed to represent the forcing uncertainties. By comparing different simulation results, the sensitivity of the upper atmosphere to the forcing uncertainties is evaluated. The results show that upper-atmospheric specification in the WACCM-X is sensitive to both types of forcing, and the ionosphere and thermosphere response to forcing uncertainties is non-linear.

1. Introduction

The coupled system of the thermosphere and ionosphere is highly nonlinear and is sensitive to the geophysical systems below and above itself. A numerical model of the thermosphere and the ionosphere that can represent the interaction between different geophysical systems is critical for space weather prediction. In numerical models, this interaction between the geophysical systems is usually determined by specified forcing parameters. Due to the missing knowledge of the mechanisms of interaction between different geophysical systems and the lack of observation of these systems' boundary, numerical models of the thermosphere and ionosphere have significant

HSU AND PEDATELLA 1 of 17

Writing – review & editing: N. M. Pedatella

inadequacies. This is compounded by the fact that the estimation of the forcings themselves are also inaccurate. These two facts lead to the growth of forecast errors in thermosphere and ionosphere weather prediction.

Therefore, it is important to understand the sensitivity of the thermospheric and ionospheric states to realistic spatiotemporal variability and uncertainty of both internal and external forcings. Based on the Monte-Carlo algorithm, ensemble simulations that quantify the flow-dependent uncertainty are a powerful method to address this issue. In an ensemble simulation experiment, a set of forcing perturbations or initial condition perturbations are generated based on *a prior* knowledge of the uncertainties in the system. This set of forcing perturbations and/or different initial condition perturbations are further applied to a series of numerical model ensembles in order to examine the sensitivity of model states to the forcings and/or initial conditions.

Lee et al. (2012) examine the sensitivity of the model of the thermosphere and ionosphere, the National Center of Atmospheric Research (NCAR) Thermosphere-Ionosphere-Electrodynamics General Circulation Model (TIE-GCM) (Qian et al., 2014; Richmond et al., 1992), to the solar irradiance, high-latitude electric potential, auroral energy flux, and lower boundary conditions. In their study, forcings of a given TIE-GCM ensemble member are parameterized to constant values, and the perturbation added to different TIE-GCM ensemble members is sampled from a Gaussian distribution. Although their result provides a general idea of the sensitivity of the TIE-GCM to the forcings, they do not quantify the true uncertainty in the forcing or the thermosphere and ionosphere state. Pedatella et al. (2018) apply ensemble simulations to TIE-GCM to understand the role of high-latitude forcing uncertainties on the low-latitude and mid-latitude ionosphere during the April 2010 geomagnetic storm period. Both the uncertainties of the high-latitude electric potential and the auroral energy flux are considered. The background high-latitude electric potential and the auroral energy flux are given by an Assimilative Mapping of Ionospheric Electrodynamics (AMIE) procedure developed by Richmond and Kamide (1988), and both the perturbations of the high-latitude electric potential and the auroral energy flux are sampled from red noise. Their study provides the first insight into the response of the low- and mid-latitude ionosphere to the uncertainty of high-latitude energy input from the magnetosphere, yet how to estimate the forcing uncertainties has still not been addressed. Hsu et al. (2021) also perturb solar irradiance, high-latitude electric potential, the auroral energy flux, and lower boundary conditions in the TIE-GCM ensemble simulations. The lower boundary conditions help determine how the lower atmosphere interacts with the thermosphere and the ionosphere. Since the lower boundary of TIE-GCM is at about 98 km altitude, instead of generated from the lower atmosphere through the atmospheric dynamics, the background tides and waves are specified using the simulation results from the Thermosphere-Ionosphere-Mesosphere-Electrodynamics General Circulation Model (TIME-GCM) (Häusler et al., 2014) driven by Modern-Era Retrospective Analysis for Research and Application (MERRA, Rienecker et al., 2011) meteorological reanalysis fields. Moreover, the uncertainty of lower-atmospheric tide and wave forcings is determined by the 30-day variability of the TIME-GCM results, meaning that this method might not be practical when the weather conditions change. Pedatella and Liu (2018) perturb lower atmosphere in a whole atmospheric model, the NCAR's Whole Atmosphere Community Climate Model with thermosphere and ionosphere eXtension (WACCM-X, Liu et al., 2018) to investigate the extent to which neglecting the realistic day-to-day lower atmospheric variability introduces uncertainty in the ionosphere response to an idealized geomagnetic storm. The lower atmospheric forcing uncertainty and variability are shown to be important for capturing smaller-scale features of the upper atmosphere response to geomagnetic storms. However, this study only focuses on a idealized storm condition with a K_p of 7 and F_{107} of 100 SFU for all 10 WACCM-X ensemble members.

This study aims to evaluate the sensitivity of the thermospheric and ionospheric states to the realistic high-latitude electric potential forcing and lower atmospheric forcing under both geomagnetic quiet and storm conditions. To estimate the uncertainty of lower atmospheric tide and wave forcings, this study adopts the WACCM-X. The data assimilative procedure, Assimilative Mapping of Geospace Observations (AMGeO, AMGeO Collaboration, 2019) is applied to compute the uncertainty of high-latitude electric potential forcing. An ensemble simulation experiment with WACCM-X and AMGeO is performed to understand the sensitivity of the thermospheric and ionospheric states to these two kinds of forcings. Sections 2.1 and 2.2 describe the WACCM-X and AMGeO in detail, Section 2.3 describes how we design the ensemble simulation experiment, and Section 2.4 explains how we determine the uncertainty of high-latitude electric potential forcing and lower atmospheric tide and wave forcing. The result and conclusion are in Sections 3 and 4.

HSU AND PEDATELLA 2 of 17

15427390, 2023, 4, Downloaded from https://agupubs.onlinelibrary.wiley.com/doi/10.1029/2022SW003216, Wiley Online Library on [11/05/2023]. See the Terms

of use; OA articles are governed by the applicable Creative Commons Licens

2. Method

2.1. WACCM-X

The numerical model used in this study is the WACCM-X. The WACCM-X is a general circulation numerical model of the whole atmosphere from the surface to pressure level 4.1×10^{-10} hPa (500–700 km altitude, depending on solar activity). The version we used in this study, WACCM-X version 2.0, is built upon the Whole Atmosphere Community Climate Model version 4 (WACCM4, Marsh et al., 2013), which itself is a vertical extension of the Community Atmosphere Model version 4 (CAM4, Neale et al., 2013). WACCM-X can self-consistently resolve lower atmospheric processes, enabling better representation of thermosphere and ionosphere weather. Compared with WACCM, the WACCM-X includes a self-consistent calculation of the low-latitude and mid-latitude electrodynamics that accounts for the neutral wind dynamo.

In the WACCM-X, the high-latitude electric potential imposed by magnetospheric processes is usually specified by a parameterized empirical ion convection model, Heelis (Heelis et al., 1982) or Weimer (Weimer, 2005), or by the data-driven model, for example, AMIE (Richmond, 1992). Meanwhile, the auroral particle precipitation is specified by an analytical auroral model (Emery et al., 2012; Qian et al., 2014). In the analytical auroral model, the average electron energy and total energy flux are computed based on the K_p index or solar wind and interplanetary magnetic field (IMF) data, and can also be determined from the other empirical models, for example, Oval Variation, Assessment, Tracking, Intensity, and Online Nowcasting (OVATION) Prime (OVATION Prime, Newell et al., 2009, 2010).

2.2. AMGeO

AMGeO, developed by AMGeO Collaboration at the University of Colorado Boulder, is a software designed to streamline data pre-processing, quality control steps, and data assimilation analysis steps for mapping of high-latitude ionospheric electrodynamics. As described in AMGeO Collaboration (2019), line-of-sight ion drifts from the Super Dual Auroral Radar Network (SuperDARN, Chisham et al., 2007) and ground magnetometer data from the SuperMAG data (Gjerloev, 2009) are downloaded, pre-processed, and used for assimilative mapping of high-latitude electric potential in the AMGeO.

After downloading and pre-processing the SuperDARN and SuperMAG data, the assimilation analysis steps are applied to estimate the high latitude electrodynamics variables. The assimilative mapping technique implemented in the AMGeO software modernizes and improves the AMIE (Richmond & Kamide, 1988). AMIE, proposed by Richmond and Kamide (1988), constructs the high-latitude electric potential pattern using spherical harmonics fitting. Matsuo et al. (2005) replace the spherical harmonic functions with Empirical Orthogonal Functions (EOFs). The SuperDARN Assimilative Mapping procedure developed by Cousins et al. (2013, 2015) applied this framework to SuperDARN and AMPERE data to estimate the high-latitude electrostatic potential and vector magnetic potential. The method that estimates the high-latitude electrostatic potential mapped from SuperDARN described in Cousins et al. (2013, 2015) is incorporated into the assimilation analysis steps in the AMGeO. More detail about the AMGeO can be found in Matsuo (2020) and references therein.

Generally, in the AMGeO, the electric potential is estimated by an Optimal Interpolation (OI) method (Cousins et al., 2015; Matsuo et al., 2005). As described in Matsuo et al. (2005), the total electric field, \mathbf{E} , includes two components: the mean electric field, \mathbf{E} and the residual electric field, \mathbf{E}' . The residual electric field can be described by a linear combination of a set of EOFs, EOF_1 , EOF_2 , ..., EOF_p as

$$\mathbf{E} = \alpha q \underbrace{FFHH}_{i} + \alpha q \underbrace{FFHH}_{i} + \dots + \alpha \alpha_{ij} \underbrace{FHHH}_{ij} \tag{1}$$

where α_1 , α_2 , ..., α_j are coefficients of EOFs. Details of how the EOFs are calculated by AMGeO can be found in Matsuo et al. (2005). According to Cousins et al. (2015), the OI cost function of the residual electric field is

$$\mathcal{J}(\mathbf{a}) = \frac{1}{2} \left[\mathbf{d} \cdot \mathbf{H} \cdot \mathbf{H} \cdot \mathbf{E} \cdot \mathbf{a}^{T} \cdot \mathbf{R} \right] \mathbf{d} \cdot \mathbf{H} \cdot \mathbf{E} \cdot \mathbf{a}^{T} \cdot \mathbf{R} \cdot \mathbf{e}^{T} \cdot \mathbf{e}^{T}$$

where $\alpha\alpha r = \alpha\alpha_1, \alpha\alpha_2, \dots, \alpha\alpha_{ij}$, P_b is a $j \times j$ matrix of background error covariance matrix, \mathbf{R} is the $i \times i$ matrix of observation error covariance, \mathbf{H} represents a linear mapping from the given EOF space to observational space,

HSU AND PEDATELLA 3 of 17

Table 1 Perturbed Forcings in Each Experiment								
Experiment	Lower atmospheric forcings	High-latitude electric potential forcing						
ENS EXP1	Adding neutrals field perturbation from 15 February	Adding electric potential perturbation from 15 March						
ENS EXP2	Adding neutrals field perturbation from 15 February	Applying non-perturb electric potential field						
ENS EXP3	Applying non-perturbed neutral fields	Adding electric potential perturbation from 15 March						

 y_{obs} and y_{model} are the vector of observations and observed state variable that is reconstructed from the model with i elements, \mathbf{x}_{model} is the model state variable, and \mathbf{d} is the discrepancy between observation and the model background. The observations, y_{abs}, used in the AMGeO includes plasma drift data from SuperDARN and geomagnetic perturbation data from SuperMAG. AMGeO uses the empirical ion convection model developed by Cousins and Shepherd (2010) with SuperDARN data (referred to hereafter as the CS10 model) as the background electric field, \mathbf{x}_{model} and the CS10 model error covariance is defined based on EOF analysis of about 2 years of SuperD-ARN observations. Under a framework proposed by Richmond and Kamide (1988), plasma drift, geomagnetic perturbation, and electric field are linearly related if the conductance are known. Therefore, we can convert background electric field from CS10 to plasma drift and geomagnetic perturbation in the observation space, y_{model}, if the Pedersen and Hall conductances are known. AMGeO's Pedersen and Hall conductances are derived through the average electron energy and energy flux using the Robinson formula (Robinson et al., 1987), and the average electron energy and energy flux are estimated based on the auroral precipitation model, OVATION Prime. H is the operator that maps the electric field from CS10 to the plasma drift and geomagnetic perturbation in the observation space, $\mathbf{y}_{model} = \mathbf{H} \mathbf{x}_{model}$. The term \mathbf{d} is the residual electric field from observation, and $\mathbf{d} - \mathbf{EOF}(\alpha)$ in Equation 2 is the difference between the residual electric field from observation and from the electric field constructed by EOFs. The α minimizing the cost function, $J(\alpha)$, is defined as the analysis coefficients of EOFs, α_{α} as

$$\mathbf{K} = \begin{bmatrix} \mathbf{H}^{T} \mathbf{R}^{1} & \mathbf{H} + \mathbf{P}_{2} \end{bmatrix}^{-1} \mathbf{H} \mathbf{R}^{1}$$
 (5)

and the analysis error covariance, P_{ω} becomes

$$\mathbf{P}_{at} = (\mathbf{I} - \mathbf{K} \mathbf{K} \mathbf{P}_{b}) \tag{6}$$

where I is the identity matrix. Detail of pre-process steps of SuperDARN and SuperMAG data can be found in (AMGeO Collaboration, 2019). This study uses the electric field analysis error covariance of electric field computed by AMGeO v1.2b as the high-latitude forcing in WACCM-X.

2.3. Ensemble Forcing Sensitivity Experiment Design

To estimate the sensitivity of the thermosphere and ionosphere to the uncertainties of different forcings, this paper presents three ensemble simulation experiments (ENS EXP1, ENS EXP2, and ENS EXP3) during the 2013 St. Patrick's Day geomagnetic storm. In each ensemble simulation experiment, 40 WACCM-X ensemble members are used, and the ionosphere-thermosphere in each ensemble member is forced by different lower atmosphere and different high-latitude electric potential patterns. The perturbed electric potential and perturbed lower atmosphere forcing are applied to WACCM-X ensemble simulations in ENS EXP1-3 as summarized in Table 1. A strong geomagnetic storm happened on 17 and 18 March 2013. As shown in Figure 1, the IMF turned southward at ~06:00 UT on 17 March and the $D_{\rm st}$ dropped down to around -130 nT at \sim 21:00 UT on 17 March (indicated by red dashed line) after the storm sudden commencement (SSC) at \sim 07:00 UT on the same day (indicated by blue dashed lines). The K_p index the days before the storm shown in Figure 1 indicates that the geomagnetic condition is quiet before the storm. This provides a good opportunity to investigate the forcing uncertainties under storm and quiet conditions and their impact on the sensitivity of the thermosphere and the ionosphere in a whole atmospheric model.

Table 1 lists the forcing perturbations that are applied in the ensemble simulation experiments. Different combinations of perturbed forcings are applied to individual ensemble members in the different experiments. Please note that this study only focuses on the uncertainty of high-latitude electric potential and the lower atmospheric

HSU AND PEDATELLA 4 of 17

15427390, 2023, 4, Downloaded from https://agupubs.onlinelibrary.wiley.com/doi/10.1029/2022SW003216, Wiley Online Library on [11/05/2023]. See the Terms and Conditions (https://onlinelibrary.wiley.com/doi/10.1029/2022SW003216, Wiley Online Library on [11/05/2023]. See the Terms and Conditions (https://onlinelibrary.wiley.com/doi/10.1029/2022SW003216, Wiley Online Library on [11/05/2023]. See the Terms and Conditions (https://onlinelibrary.wiley.com/doi/10.1029/2022SW003216, Wiley Online Library on [11/05/2023]. See the Terms and Conditions (https://onlinelibrary.wiley.com/doi/10.1029/2022SW003216, Wiley Online Library on [11/05/2023]. See the Terms and Conditions (https://onlinelibrary.wiley.com/doi/10.1029/2022SW003216, Wiley Online Library.wiley.com/doi/10.1029/2022SW003216, Wiley Online Library.wiley.com/doi/10.1029/2022SW00325, Wiley Online Library.wiley.com/doi/10.1029/2022SW00325, Wiley Online Library.wiley.com/doi/10.1029/2022SW00325, Wiley O

conditions) on Wiley Online Library for rules

of use; OA articles are governed by the applicable Creative Commons License

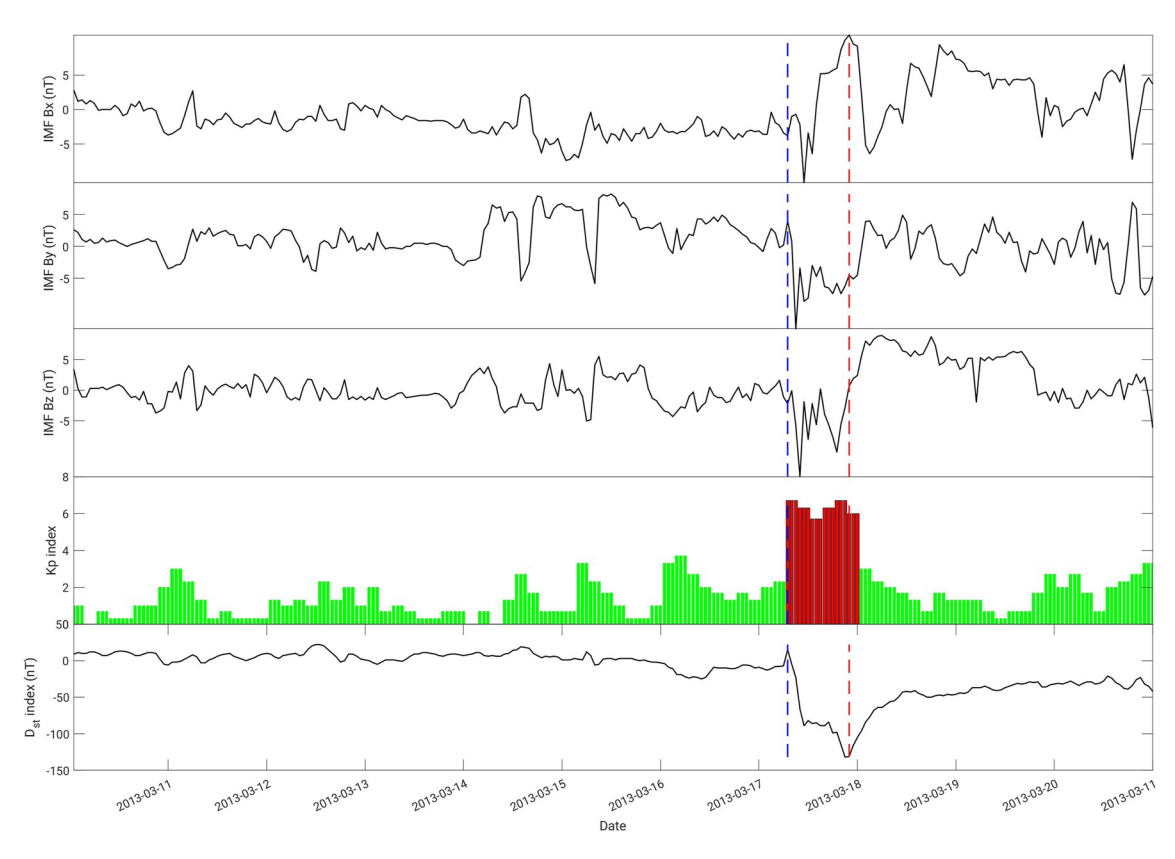


Figure 1. From top to bottom are the interplanetary magnetic field B_x , B_y , and B_z component, K_p index, and D_{st} index from 00:00 UT of 10 March 2013 to 00:00 UT of 21 March 2013. Blue and red dashed lines indicate 07:00 and 21:00 UT of 17 March 2013.

forcings, so the auroral particle precipitation is the same among all ensemble members in all experiments. Figure 2 shows the average electron energy and total energy flux before and after the storm at 23:00 UT on 15 and 17 March. This average electron energy and total energy flux are the same among all ensemble members in all experiments. The ENS EXP2 is designed to evaluate the sensitivity of the thermosphere and ionosphere in the WACCM-X to uncertainty of lower atmospheric forcings. In ENS EXP2, the method mentioned in the following sub-section is applied to perturb the lower atmosphere. The high-latitude electric potential computed by the Heelis ion convectional model and the auroral particle precipitation computed by the analytical auroral model are driven by the real K_n index and are applied to all ensemble members during 00:00 UT on 15 February to 00:00 UT on 15 March 2013. After that, AMGeO electric potential and auroral particle precipitation computed by OVATION Prime are applied to storm period simulation. ENS EXP3 is designed to evaluate the sensitivity of the thermosphere and ionosphere in the WACCM-X to uncertainty of the high-latitude electric potential. In ENS EXP3, a set of perturbed high-latitude electric potential fields generated by the method described in the next sub-section is applied to ensemble members after 00:00 UT on 15 March 2013, and the lower atmosphere and auroral particle precipitation (computed by OVATION Prime) are the same in all ensemble members. Note that the lower atmosphere is constrained to the MERRA2 reanalysis in ENS EXP3 to ensure it is identical among all ensemble members. In addition, both the perturbations of lower atmospheric neutral fields and high-latitude electric potential are applied to ENS EXP1 to examine the sensitivity of WACCM-X when both kinds of uncertainties are taken into account.

2.4. Forcing Uncertainty Estimation Method

Assuming that there are I WACCM-X ensemble members, indexed as i = 1, ..., I, and each WACCM-X ensemble member has a specific set of external forcings, $\mathbf{f}^{(i)}$, the ith ensemble model state, $\mathbf{x}^{(i)}$, advanced from time t to t+1 is

$$\mathbf{x}^{ij}(t+1) = \square_t \, \mathbf{x}^{ij}(t), \, \mathbf{f}^{ij}(t), \qquad (7)$$

HSU AND PEDATELLA 5 of 17

15427390, 2023. 4, Downloaded from https://agupubs.onlinelibrary.wiley.com/doi/10.1029/2022SW003216, Wiley Online Library on [11/05/2023]. See the Terms and Conditions (https://onlinelibrary.wiley.com/

of use; OA articles are governed by the applicable Creative Commons Licens

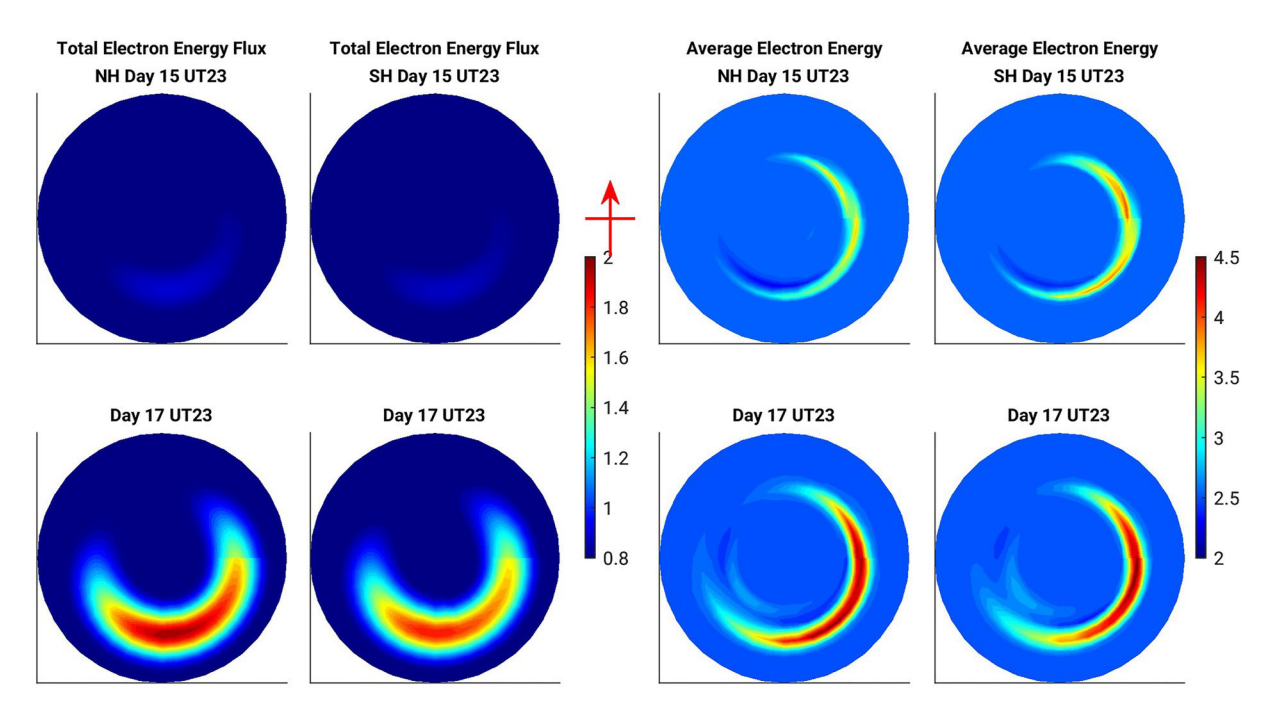


Figure 2. Average electron energy and total energy flux at 23:00 UT on 15 and 17 March. The top panels are the average electron energy and total energy flux at 23:00 UT on 15 March, and the bottom panels are that on 17 March. The first column is the total energy flux in the northern hemisphere in ergs/cm²/s; the second column is the total energy flux in the southern hemisphere ergs/cm²/s; the third column is the average electron energy in the northern hemisphere in keV; The first column is the average electron energy in the southern hemisphere in keV. The red arrow indicate the Sun-Earth direction.

where the $\mathbf{x}^{(t)}(t)$ is the initial model state of the ith member at time t, the $\mathbf{x}^{(t)}(t+1)$ is the model state of the ith member at time t+1, and \square_t is the time-integrated operator represented by the WACCM-X. Both $\mathbf{x}^{(t)}(t)$ and $\mathbf{x}^{(t)}(t+1)$ are vectors that include model state variables on the 3-dimensional model grid. $\mathbf{x}^{(t)}(t)$ is constructed by the ensemble mean term (average among model ensemble members), $\mathbf{x}^{(t)}(t)$, and the perturbed term, $\mathbf{x}^{(t)}(t)$, as

$$\mathbf{x}(\mathbf{z} = \mathbf{x}\mathbf{z} + \mathbf{x}^{\mathbf{z}}(\mathbf{z}.$$

To estimate the impact of uncertainty of lower atmospheric forcings on the uncertainty of the thermosphere and ionosphere, Gaussian noise was added to the neutral zonal and meridional wind and temperature fields at the beginning of ENS EXP1 and ENS EXP2, $t = t_0$. The standard deviation (STD) of Gaussian noise that added to the wind fields is 0.1 m/s and that added to the temperature is 0.1 K. In our case, t_0 is 00:00 UT on 15 February 2013. After a 1-month spin-up period from 15 February to 15 March, internal model dynamics leads to chaotic growth from the initial perturbations that ultimately results in the representation of the lower atmosphere forcing on the thermosphere and ionosphere being different in each ensemble member (Pedatella & Liu, 2018). For ENS EXP1 and ENS EXP2, the elements in vector $\mathbf{x} \in (\mathcal{S})$ that are related to the lower atmospheric neutral zonal and meridional wind fields and neutral temperature are Gaussian noise, and other elements are zeros. For ENS EXP3, all elements in $\mathbf{x} \in (\mathcal{S})$ are zeros.

f(i) (*t*) is a vector of WACCM-X external forcings of the *i*th member, which in this study is the high-latitude electric field, $\mathbf{E}^{(i)}(\mathbf{a}) = \mathbf{E}^{(i)}(\mathbf{a}) + \mathbf{E}^{(i)}(\mathbf{a})$. Each ensemble member has a specific $\mathbf{E}^{(i)}(\mathbf{a})$, but $\mathbf{E}(\mathbf{a})$ is the same among all ensemble members. Before 00:00 UT of 15 March 2013, $\mathbf{E}(\mathbf{a})$ is given by Heelis ion convectional model and is switched to AMGeO after that. For ENS EXP2, all elements in $\mathbf{E}^{(i)}(\mathbf{a})$ are zeros. For ENS EXP1 and ENS EXP3, all elements in $\mathbf{E}^{(i)}(\mathbf{a})$ before 00:00 UT of 15 March 2013 are zeros, and are randomly drawn from the multivariate normal distribution with AMGeO's analysis error covariance, \mathbf{P}_a , after 00:00 UT of 15 March 2013. The high-latitude electric field perturbation of the *i*th ensemble member is

$$\mathbf{E}^{\hat{A}}(\hat{A}) = \alpha \hat{A}^{\hat{A}}(\hat{A}) \underbrace{EEEEEE_{\hat{A}}}_{1} + \alpha \hat{A}^{\hat{A}}(\hat{A}) \underbrace{EEEEEE_{\hat{A}}}_{2} + \dots + \alpha \hat{A}^{\hat{A}}(\hat{A}) \underbrace{EEEEEE_{\hat{A}}}_{\hat{A}}$$
(9)

$$d\vec{t}(t \sim M(a q_{\alpha} \mathbf{H}_{\alpha}(t)). \tag{10}$$

HSU AND PEDATELLA 6 of 17

15427390, 2023, 4, Downloaded from https://agupubs.onlinelibrary.wiley.com/doi/10.1029/2022SW003216, Wiley Online Library on [11/05/2023]. See the Terms and Conditions (https://agupubs.onlinelibrary.wiley.com/doi/10.1029/2022SW003216, Wiley Online Library on [11/05/2023]. See the Terms and Conditions (https://agupubs.onlinelibrary.wiley.com/doi/10.1029/2022SW003216, Wiley Online Library on [11/05/2023]. See the Terms and Conditions (https://agupubs.onlinelibrary.wiley.com/doi/10.1029/2022SW003216, Wiley Online Library on [11/05/2023]. See the Terms and Conditions (https://agupubs.onlinelibrary.wiley.com/doi/10.1029/2022SW003216, Wiley.com/doi/10.1029/2022SW003216, Wiley

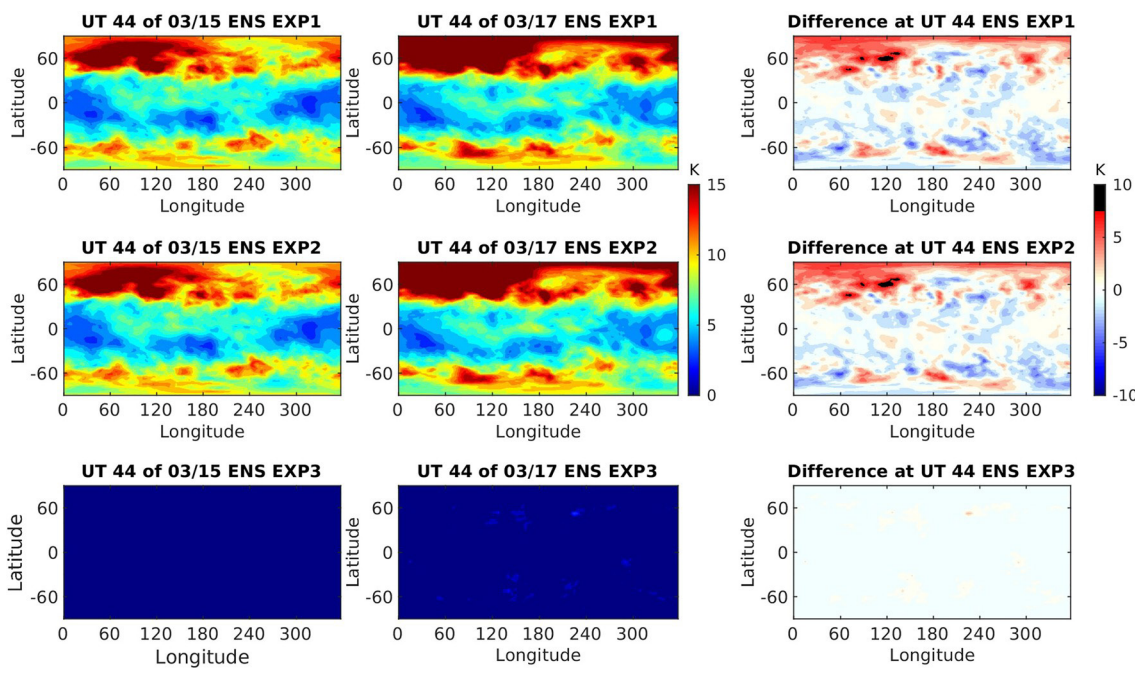


Figure 3. The standard deviation (STD) of neutral temperature wind computed from the WACCM-X ensemble at about 0.013 hPa pressure level (about 80 km altitude). From top to bottom are results from ENS EXP1, ENS EXP2, and ENS EXP3. The first and second columns are the STD of the WACCM-X ensemble at 23:00 UT of 15 and 17 March, respectively. The third column is the difference between the STD at 23:00 UT of 15 and 17 March. The red scale in the third column's subplots means that the STD at 23:00 UT of March 17 is larger than that at 23:00 UT of 15 March; the blue scale means that the STD at 23:00 UT of 17 March is smaller than that at 23:00 UT of 15 March.

These perturbed electric fields help estimate the uncertainty of electric potential with current knowledge of the empirical model and SuperDARN and SuperMAG data. The sensitivity of the thermosphere and ionosphere to the uncertainties of low-atmospheric wave and tide forcings and high-latitude electric potential can now be estimated by driving a set of the WACCM-X ensemble with these two kinds of perturbations based on the Monte-Carlo algorithm.

3. Result

In this section, we first demonstrate the perturbed forcings determined by the method described in Section 2.4, and then show the sensitivity of both thermosphere and ionosphere in the WACCM-X due to the perturbed forcings.

Figure 3 is the longitude-latitude maps of the STD of neutral temperature computed from ensemble members at about 0.013 hPa pressure level, which is approximately 80 km altitude. Similar figures for neutral zonal wind and neutral meridional wind, Figures S1 and S2 can be found in Supporting Information S1. Left to right columns of these figures show the STD at 23:00 UT of 15 and 17 March and the difference of STD between these two times, respectively, representing the STD before and after SSC and the change of STD due to the geomagnetic storm.

Generally, large uncertainties of neutral zonal wind, neutral meridional wind, and neutral temperature are seen in ENS EXP1 and ENS EXP2 before SSC. The STD of zonal and meridional neutral wind fields from ensemble members in ENS EXP1 and ENS EXP2 that include lower atmospheric perturbation can reach about 50 m/s at mid-latitudes in the northern hemisphere, and the STD of temperature can reach about 15 K. In contrast, the STDs of these three fields are almost zero in ENS EXP3 during quiet time. The ensemble members fully diverge over the 1-month spin-up period leading to the large ensemble STD shown before SSC in ENS EXP1 and ENS EXP2. After SSC, the STDs of these three fields in ENS EXP3 increase a little, and the changes of STDs of ENS EXP1 and ENS EXP2 are more complex (increase in some places and decrease in others). This would suggest that the strong high-latitude forcings might strengthen the spread caused by the uncertainties from the lower atmosphere, even at 80 km. More studies about this mechanism might need to be addressed in the future.

HSU AND PEDATELLA 7 of 17

15427390, 2023, 4, Downloaded from https://agupubs.onlinelibrary.wiley.com/doi/10.1029/2022SW003216, Wiley Online Library on [11/05/2023]. See the Terms and Conditions (https://onlinelibrary.wiley.com/doi/10.1029/2022SW003216, Wiley Online Library on [11/05/2023]. See the Terms and Conditions (https://onlinelibrary.wiley.com/doi/10.1029/2022SW003216, Wiley Online Library on [11/05/2023]. See the Terms and Conditions (https://onlinelibrary.wiley.com/doi/10.1029/2022SW003216, Wiley Online Library on [11/05/2023]. See the Terms and Conditions (https://onlinelibrary.wiley.com/doi/10.1029/2022SW003216, Wiley Online Library on [11/05/2023]. See the Terms and Conditions (https://onlinelibrary.wiley.com/doi/10.1029/2022SW003216, Wiley Online Library.wiley.com/doi/10.1029/2022SW003216, Wiley Online Library.wiley.com/doi/10.1029/2022SW003250, Wiley Online Library.wiley.com/doi/10.1029/2022SW0032SW003250, Wiley Online Library.wiley.com/doi/10.1029/2022SW003250

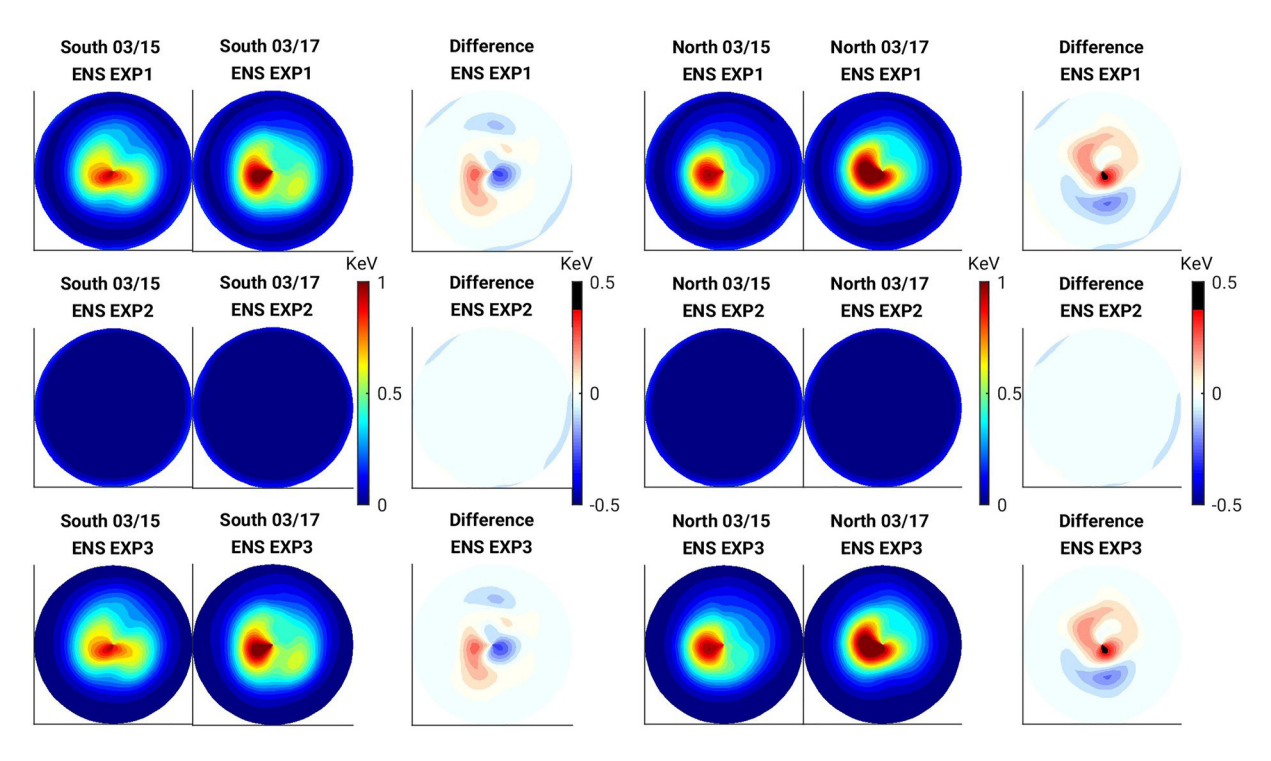


Figure 4. The standard deviation (STD) of electric potential from the WACCM-X ensemble. From top to bottom are results from ENS EXP1, ENS EXP2, and ENS EXP3. The first and second columns are the STD of the southern hemispheric electric potential from the WACCM-X ensemble at 23:00 UT of 15 and 17 March, respectively. The third columns is the difference of the STD of the southern hemispheric electric potential at 23:00 UT of 15 and 17 March. The fourth and fifth columns are the STD of the northern hemispheric electric potential from the WACCM-X ensemble at 23:00 UT of 15 and 17 March, respectively. The sixth column is the difference of the STD of the northern hemispheric electric potential at 23:00 UT of 15 and 17 March. The red scale in the third and sixth columns' subplots represents that the STD at 22:00 UT of 17 March is larger than that at 23:00 UT of 15 March; the blue scale represents that the STD at 23:00 UT of 17 March is smaller than that at 23:00 UT of 15 March.

Figure 4 is the STD of electric potential over the northern and southern hemispheres. The ENS EXP1 and ENS EXP3, including high-latitude electric potential perturbation, show large STDs. The STD increases after SSC while the energy input from the magnetosphere increases. This aligns with the fact that the geomagnetic storm will raise the uncertainty of high-latitude electric potential forcings. Most data used in the AMGeO are from the northern hemisphere, and the estimation in the southern hemisphere might not be as accurate as in the northern hemisphere. Furthermore, the STD of electric potential is about 5% of the background electric potential, indicating the uncertainty of the AMGeO estimated electric potential is relatively small if assumptions behind the method of AMGeO are correct.

Figure 5 shows the latitude-altitude maps of the ensemble STD of the amplitude of diurnal westward propagating tide with zonal wavenumber 1 (DW1), semidiurnal westward propagating tide with zonal wavenumber 2 (SW2), and diurnal eastward propagating tide with zonal wavenumber 3 (DE3) in neutral temperature computed from the ENS EXP2 and ENS EXP3 WACCM-X ensemble before SSC. Similar figures for neutral zonal wind and neutral meridional wind, Figures S3 and S4 can be found in Supporting Information S1. Results for ENS EXP1 are similar to ENS EXP2 and are not shown. The ensemble STD of DW1, SW2, and DE3 are computed using the hourly WACCM-X output from 15 to 19 March. These Figures help quantify the uncertainty of tideal forcing from the lower atmosphere to the thermosphere and the ionosphere. Generally, the results are consist with Figure 3, Figures S1 and S2 in Supporting Information S1. Large STD of DW1, SW2, and DE3 components are shown in ENS EXP2. In contrast, the STD of DW1, SW2, and DE3 components from ENS EXP3 are negligible, revealing that the uncertainty of lower atmospheric tide and wave forcings are successfully applied to ENS EXP1 and ENS EXP2 with the help of lower atmospheric perturbation method we described in the previous section.

Figures 3–5 and Figures S1–S4 in Supporting Information S1 demonstrate how the uncertainties of lower atmospheric forcings and high-latitude electric potential forcing estimated with the methods outlined in the previous section look like, and next, the impact of these uncertainties on the thermosphere and the ionosphere will be addressed.

HSU AND PEDATELLA 8 of 17

15427390, 2023, 4, Downloaded from https://agupubs.onlinelibrary.wiley.com/doi/10.1029/2022SW003216, Wiley Online Library on [11/05/2023]. See the Terms and Conditions (https://onlinelibrary.wiley.com/errms

and-conditions) on Wiley Online Library for rules

of use; OA articles

emed by the applicable Creative Commons License

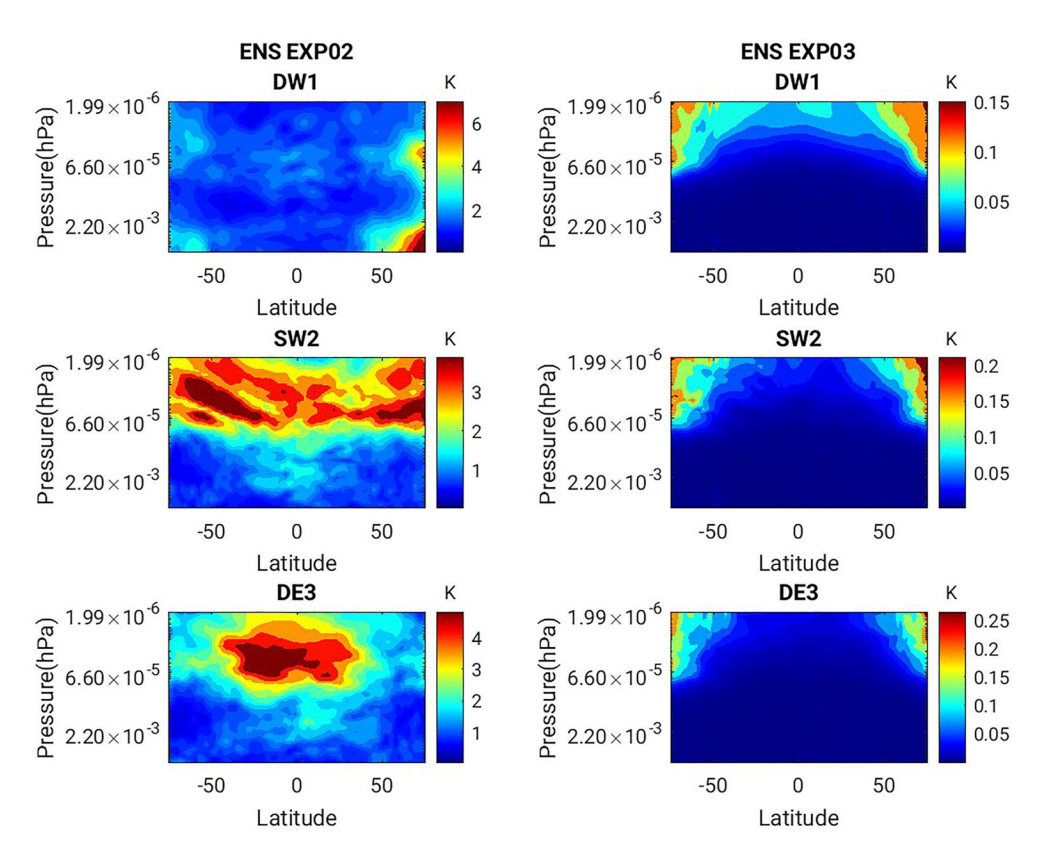


Figure 5. Latitude-altitude maps of the ensemble standard deviation of the amplitude of diurnal westward propagating tide with zonal wavenumber 1 (DW1, top panels), semidiurnal westward propagating tide with zonal wavenumber 2 (SW2, middle panels), and diurnal eastward propagating tide with zonal wavenumber 3 (DE3, bottom panels) in neutral temperature computed from the ENS EXP2 (left column) and ENS EXP3 (right column) WACCM-X ensemble before storm sudden commencement.

We use the average STD to quantify the impact of the uncertainties on the thermosphere and ionosphere as

$$\sigma(t) = \frac{1}{N} \sum_{n=1}^{N} \sqrt{\frac{1}{\Gamma}} \left(xx(tt)_{\text{lim}} - \bar{x}(tt)_{n} \right)^{2}$$

$$(11)$$

where $\alpha(t)$ is the averaged STD of a given model state at time t, n is the index of model grid, N is the number of horizontal WACCM-X model grid in the region that we focus on, i is the index of model ensemble, I is the total number of model ensembles (I = 40 in this study), $x(t)_{in}$ is the model state variable from ith ensemble at time t, and $x(t)_{in}$ is the ensemble mean of model state variable at model time t. Equation 11 is applied to different model states to evaluate the impact of the uncertainties of difference forcings on the thermospheric and ionospheric states.

Figure 6 shows the averaged STDs of temperature, zonal wind, meridional wind, and vertical total electron content (TEC) at high-latitudes (poleward of 60°) from 00:00 UT of 15 March to 00:00 UT of 19 March. The averaged STDs of temperature, zonal wind, and meridional wind are computed from the temperature, zonal wind, and meridional wind states at 4.687×10^{-8} hPa pressure level (about 350 km altitude). The values shown in Figure 6 and the follow-on figures (Figures 7–9) are considerably smaller than the background model states because they are averaged over all model grids, but the STDs can reach a considerably larger value in particular locations, which will be discussed later. At the beginning of the experiment, the averaged STDs of all states from ENS EXP1 (red lines) and ENS EXP2 (blue lines) are the same and larger than that from ENS EXP3 (black lines). This is because both ENS EXP1 and ENS EXP2 are initialized from the same initial ensemble set that includes lower atmospheric perturbation, and ENS EXP3 has not been perturbed at the beginning. Starting from 00:00 UT of 15 March, the high-latitude electric potential perturbation added to the ENS EXP1 and ENS EXP3 brings the

HSU AND PEDATELLA 9 of 17

15427390, 2023, 4, Downloaded from https://agupubs.onlinelibrary.wiley.com/doi/10.1029/2022SW003216, Wiley Online Library on [11/05/2023]. See the Terms and Conditions (https://onlinelibrary.wiley

onditions) on Wiley Online Library for rules of use; OA articles are governed by the applicable Creative Commons License

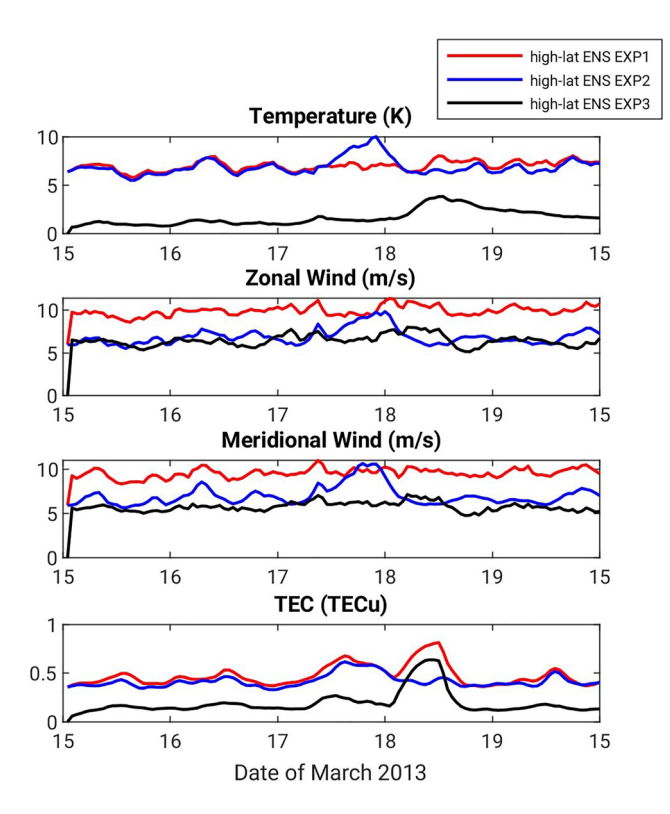


Figure 6. Temporal variation of the high-latitude (poleward of 60° N or 60° S) averaged standard deviation (STD) computed from WACCM-X ensemble over the period between 00:00 UT of 15 March and 00:00 UT of 19 March. Top to third panels are STD of neutral temperature, neutral zonal wind, and neutral meridional wind at 4.687×10^{-8} hPa pressure level (about 350 km altitude) averaged over high-latitude WACCM-X model grids. The fourth panel is the STD of total electron content averaged over high-latitude WACCM-X model grids. Red, blue, and black lines are STD computed from ENS EXP1, ENS EXP2, and ENS EXP3, respectively.

averaged STDs of both thermospheric and ionospheric states from these two experiments higher. STDs of ENS EXP2 are overall larger than ENS EXP3 indicating that the influence of the lower atmosphere forcing uncertainty is relatively large compared to the electric potential forcing uncertainty determined by AMGeO. During the storm time, the uncertainty of electric potential forcing strongly impacts the STDs of Joule heating and further changes the temperature, zonal wind, meridional wind fields in the high-latitude thermosphere and TEC in the high-latitude ionosphere. The averaged STD of all states from ENS EXP1 is overall larger than the other two, implying that the high-latitude averaged STD of states from ENS EXP1 is a superimposed effect of the uncertainties of the lower-atmospheric forcings and high-latitude electric potential forcing.

By averaging the STDs over all horizontal grids, Figure 7 shows the vertical profiles of the high-latitude averaged STDs of temperature, neutral zonal wind, and neutral meridional wind at 12:00 UT of 15 and 18 March in dashed and solid lines. The averaged STDs from ENS EXP1 and ENS EXP2 are mostly overlapped in the troposphere and stratosphere at both 12:00 UT of 15 and 18 March because we use the same lower atmospheric perturbation in these two experiments. The values increase along with altitude and reach a maximum in the mesosphere-lower thermosphere region. The increasing dissipation in the thermosphere leads to a reduction in the STD above \sim 10⁻⁴ hPa, possibly implying that only part of the lower-atmospheric energy is propagated upward to the thermosphere. On the other hand, the averaged STDs from ENS EXP3 are almost zero in the lower atmosphere and increase along with the altitude. The averaged STDs from ENS EXP3 is still smaller than ENS EXP2, indicating that the impact of uncertainty of the high-latitude electric potential forcing determined by AMGeO is smaller than the impact of the uncertainties of lower atmospheric forcings. The averaged STDs from ENS EXP1 are again slightly larger than that from ENS EXP2, indicating the combining effect of both the uncertainties of lower atmospheric forcings and high-latitude electric potential forcing appears in the ENS EXP1. The averaged STDs from ENS EXP1 and ENS EXP3 after SSC are larger than that before SSC (except the STD of temperature from ENS EXP1), which is consistent with Figure 6.

The dayside low-latitude region TEC is mainly contributed by the F-region Equatorial Ionization Anomaly (EIA), which is highly related to both the neutral states (neutral zonal wind) and the ionized states (vertical plasma drift). To investigate the connection between the sensitivity of these states, Figure 8 shows the averaged STDs of zonal wind at 4.687×10^{-8} hPa pressure level (about 350 km altitude), vertical plasma drift at geomagnetic equator, and TEC in the low-latitude region from 00:00 UT of 15 March to 00:00 UT of 19 March. The averaged STDs of all states from ENS EXP1 and ENS EXP2 are significantly larger than that from ENS EXP3 over the whole experiment period, indicating that the low-latitude thermospheric and ionospheric states are considerably impacted by the lower atmospheric forcings. The averaged STDs of zonal wind states from ENS EXP3 slightly increase a couple of hours after the SSC and peak at about 12:00 UT on 18 March. Perturbed high-latitude electric potential forcing in different ensemble members causes differences in the magnitude of Joule heating, leading to different equatorward neutral wind patterns in the upper atmosphere. These results demonstrate that high-latitude electric potential forcing uncertainty is less important to the equatorial vertical plasma drift under geomagnetic quiet conditions. After the SSC, a peak of the averaged STDs of equatorial vertical plasma drift from ENS EXP3 appears. This indicates that the prominent variability of thermospheric wind, shown as the peak of averaged STDs of zonal wind from ENS EXP3, changes the electrodynamic processes and increases the averaged STDs of equatorial vertical plasma drift during the storm time. Finally, for ENS EXP3, the behavior of the averaged STDs of TEC before and after SSC are similar to the averaged STDs of equatorial plasma drift and zonal wind, indicating the sensitivity of the low-latitude electron density distribution is highly related to the sensitivity of equatorial plasma drift and the sensitivity of thermospheric zonal winds.

HSU AND PEDATELLA 10 of 17

15427390, 2023, 4, Downloaded from https://agupubs.onlinelibrary.wiley.com/doi/10.1029/2022SW003216, Wiley Online Library on [11/05/2023]. See the Terms and Conditions (http

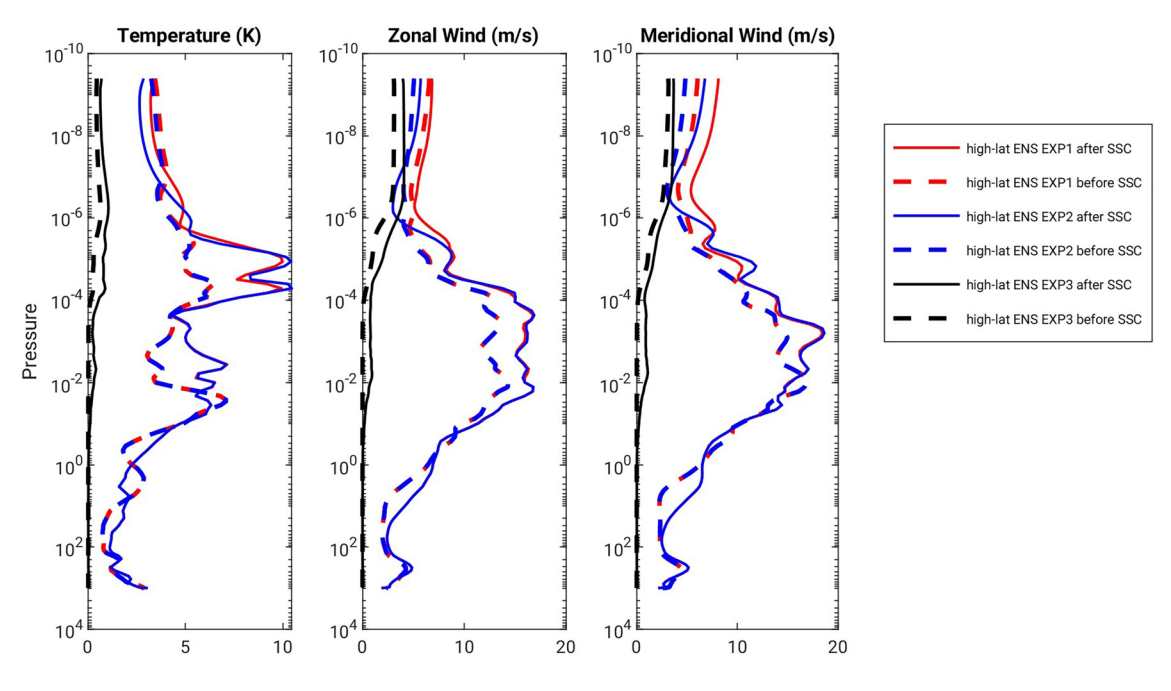


Figure 7. Vertical profiles of the high-latitude averaged standard deviation (STD) computed from WACCM-X ensemble before and after storm sudden commencement. Left to right panels are the STD of neutral temperature, zonal wind, and meridional wind averaged over high-latitude horizontal model grids at each model level. Dash and solid lines are the profiles at 12:00 UT of 15 and 18 March. Red, blue, and black lines are averaged STD computed from ENS EXP1, ENS EXP2, and ENS EXP3, respectively.

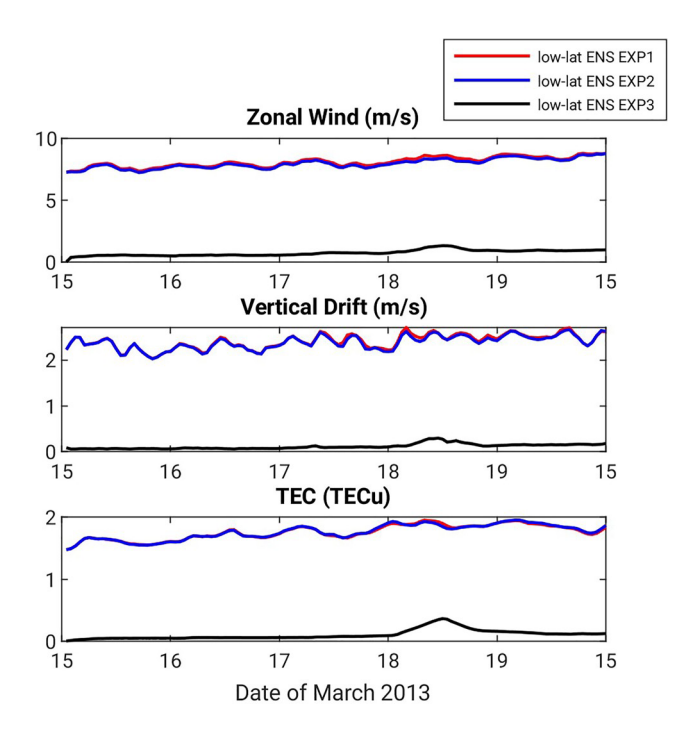


Figure 8. Temporal variation of the low-latitude ($\pm 60^{\circ}$) averaged standard deviation (STD) computed from WACCM-X ensemble over the period between 00:00 UT of 15 March and 00:00 UT of 19 March. Top to bottom panels are STD of neutral zonal wind at 4.687×10^{-8} hPa pressure level (about 350 km altitude), vertical plasma drift at geomagnetic equator, and total electron content averaged over low-latitude WACCM-X model grids. Red, blue, and black lines are averaged STD computed from ENS EXP1, ENS EXP2, and ENS EXP3, respectively.

Figure 9 also shows the vertical profiles of low-latitude averaged STDs of neutral temperature, neutral zonal wind, and neutral meridional wind at 12:00 UT of 15 and 18 March. Since the TEC is vertical integrated electron density and equatorial vertical plasma drift mainly does not have much vertical variation between the E region and F2 region, we only show the vertical profiles of neutral temperature, neutral zonal wind, and neutral meridional wind. Similar to Figure 7, a maximum of averaged STD from ENS EXP1 and ENS EXP2 is also shown in the mesosphere-lower thermosphere region. Overall, the averaged STDs from ENS EXP3 are considerably smaller compared with that from the other two experiments, indicating the sensitivity of low-latitude thermospheric states are dominated by the uncertainty of the lower atmospheric forcings.

In addition, Table 2 lists the value of averaged STD at 12:00 UT on 15 and 18 March plotted in Figures 6 and 8 so the changes of the uncertainty in the lowand high-latitude regions before and after the storm can be compared easily. It is clear that the STD from the ENS EXP1 is larger than the STD from the other two experiments. The sum of STD from the ENS EXP2 and ENS EXP3 is not equal to STD from the ENS EXP1, implying the contributions of the uncertainties of high-latitude electric potential and lower-atmospheric waves and tides cannot be distinguished linearly.

We further demonstrate the spatial sensitivity of the thermosphere and ionosphere states to different forcings. Figures 10–12 are longitude-latitude maps of the STDs of neutral zonal wind, neutral meridional wind, and neutral temperature computed from model ensembles at 4.687×10^{-8} hPa pressure level. Figure 13 is longitude-latitude maps of the STDs of TEC, and Figure 14 is the STDs of vertical plasma drift along geomagnetic equator.

The left to right of Figures 10–13 are the longitude-latitude map of the STDs at 12:00 UT of 15, that at 12:00 UT of 18 March, and the difference between

HSU AND PEDATELLA 11 of 17

15427390, 2023, 4, Downloaded from https://agupubs.onlinelibrary.wiley.com/doi/10.1029/2022SW003216, Wiley Online Library on [11/05/2023]. See the Terms and Conditions (https://agupubs.onlinelibrary.wiley.com/doi/10.1029/2022SW003216, Wiley Online Library on [11/05/2023]. See the Terms and Conditions (https://agupubs.onlinelibrary.wiley.com/doi/10.1029/2022SW003216, Wiley Online Library on [11/05/2023]. See the Terms and Conditions (https://agupubs.onlinelibrary.wiley.com/doi/10.1029/2022SW003216, Wiley Online Library on [11/05/2023]. See the Terms and Conditions (https://agupubs.onlinelibrary.wiley.com/doi/10.1029/2022SW003216, Wiley Online Library on [11/05/2023]. See the Terms and Conditions (https://agupubs.onlinelibrary.wiley.com/doi/10.1029/2022SW003216, Wiley Online Library on [11/05/2023]. See the Terms and Conditions (https://agupubs.onlinelibrary.wiley.com/doi/10.1029/2022SW003216, Wiley Online Library on [11/05/2023]. See the Terms and Conditions (https://agupubs.onlinelibrary.wiley.com/doi/10.1029/2022SW003216, Wiley Online Library.wiley.com/doi/10.1029/2022SW003216, Wiley Online Library.wiley.wiley.com/doi/10.1029/2022SW003216, Wiley Online Library.wiley.com/doi/10.1029/2022SW003216, Wiley Online Library.wiley.com/doi/10.1029/2022SW003216, Wiley Online Library.wiley.com/doi/10.1029/2022SW003216, Wiley Online Library.wiley.wiley.com/doi/10.1029/2022SW003216, Wiley Online Library.wiley.wi

nditions) on Wiley Online Library for rules of use; OA articles are governed by the applicable Creative Commons License

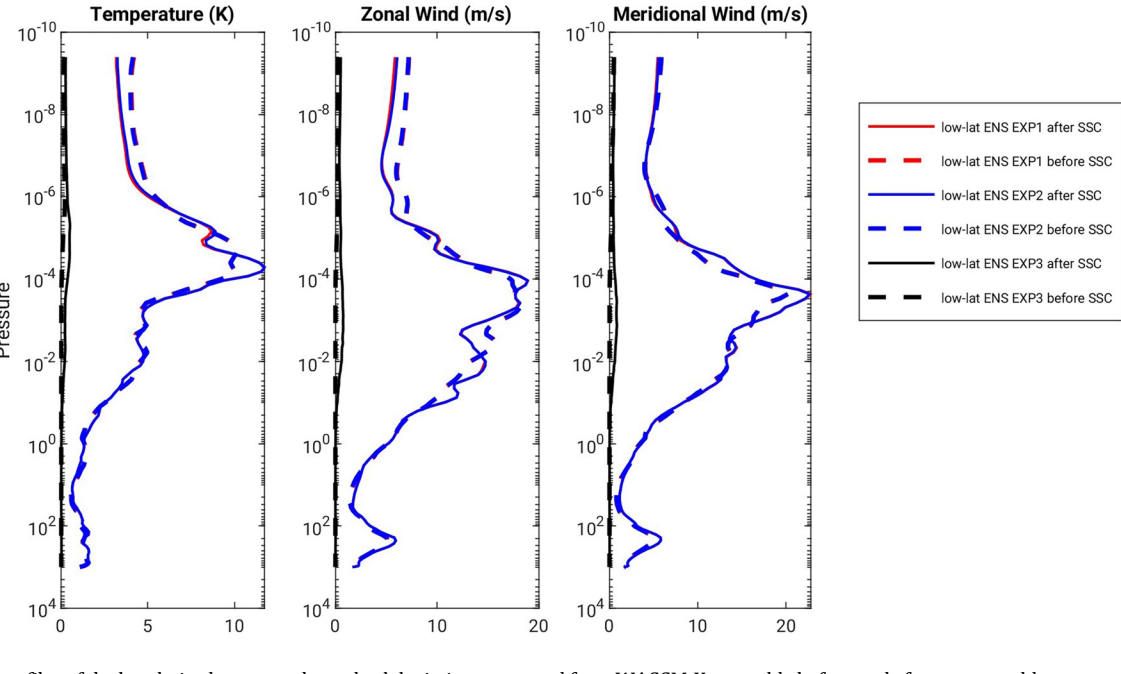


Figure 9. Vertical profiles of the low-latitude averaged standard deviation computed from WACCM-X ensemble before and after storm sudden commencement. Similar to 7 but for low-latitude region.

this two times. The results shown in Figures 10-14 are generally consistent with the results shown in Figures 6-9. In ENS EXP1, the high-latitude STDs of all neutral states are larger than the low-latitude STDs. The maximum high-latitude STD of neutral zonal wind at 4.687×10^{-8} hPa pressure level reaches 21.38 and 27.90 m/s at 12:00 UT of 15 and 18 March, respectively, and the maximum low-latitude STD of neutral zonal wind reaches 15.64 m/s and 18.01 m/s. The maximum high-latitude STD of neutral meridional wind reaches 23.23 m/s and 32.75 m/s, and the maximum low-latitude STD of neutral meridional wind reaches 13.75 m/s and 14.18 m/s. The maximum high-latitude STD of neutral temperature reaches 10.44 and 12.78 K, and the maximum low-latitude STD of neutral temperature reaches 11.74 and 11.27 K. In addition, a sharp gradient between high and low latitude are shown around auroral oval in Figures 10-12 in ENS EXP1 and ENS EXP3. This is mainly due to the treatment of high-latitude convection pattern determined by AMGeO that is separated from the mid- and low-latitude dynamo in the WACCM-X. On the other hand, the STDs of TEC in the low-latitude region are significantly larger than those in the high-latitude region because of the contribution of the EIA. The maximum high-latitude STD of TEC reaches 1.20 TECu and 1.51 TECu at 12:00 UT of 15 and 18 March, and the maximum low-latitude STD of TEC reaches 6.50 TECu and 6.85 TECu. The maximum STD of the equatorial vertical plasma drift reaches 0.14 m/s and 0.72 m/s at 12:00 UT of 15 and 18 March. In ENS EXP2, the main STDs structure mainly appears in the low-latitude region, while the STDs structure primarily appears in the high-latitude region in the ENS EXP3. This is clearly because of different perturbed forcings in experiments.

Table 2 Averaged Standard Deviation at 12:00 UT of 15 and 18 March at 4.687×10^{-8} hPa Pressure Level in Figures 6 and 8

		ENS EXP1		ENS EXP2		ENS EXP3	
Variable	Latitude	15 March	18 March	15 March	18 March	15 March	18 March
Temperature (K)	Low	6.09	6.60	6.08	6.37	0.26	2.17
	High	6.15	7.96	5.98	6.46	0.98	3.83
Zonal Wind (m/s)	Low	7.51	8.61	7.42	8.38	0.55	1.30
	High	8.89	10.16	5.69	6.00	6.04	7.12
Meridional wind	Low	7.61	7.76	7.53	7.64	0.54	1.27
(m/s)	High	8.35	9.65	5.68	6.08	5.25	6.16

HSU AND PEDATELLA 12 of 17

15427990, 2023, 4, Downloaded from https://agupubs.onlinelibrary.wiley.com/doi/10.1029/20225W003216, Wiley Online Library on [11/05/2023]. See the Terms and Conditions (https://onlinelibrary.wiley.com/terms-and-conditions) on Wiley Online Library for rules of use; OA articles are governed by the applicable Creative Commons and Conditions (https://onlinelibrary.wiley.com/terms-and-conditions) on Wiley Online Library for rules of use; OA articles are governed by the applicable Creative Commons and Conditions (https://onlinelibrary.wiley.com/terms-and-conditions) on Wiley Online Library for rules of use; OA articles are governed by the applicable Creative Commons and Conditions (https://onlinelibrary.wiley.com/terms-and-conditions) on Wiley Online Library for rules of use; OA articles are governed by the applicable Creative Commons and Conditions (https://onlinelibrary.wiley.com/terms-and-conditions) on Wiley Online Library for rules of use; OA articles are governed by the applicable Creative Commons and Conditions (https://onlinelibrary.wiley.com/terms-and-conditions) on Wiley Online Library for rules of use; OA articles are governed by the applicable Creative Commons and Conditions (https://onlinelibrary.wiley.com/terms-and-conditions) on Wiley Online Library for rules of use; OA articles are governed by the applicable Creative Commons and Conditions (https://onlinelibrary.wiley.com/terms-and-conditions) on the applicable Creative Commons (https://onlinelibrary.wiley.com/terms-and-c

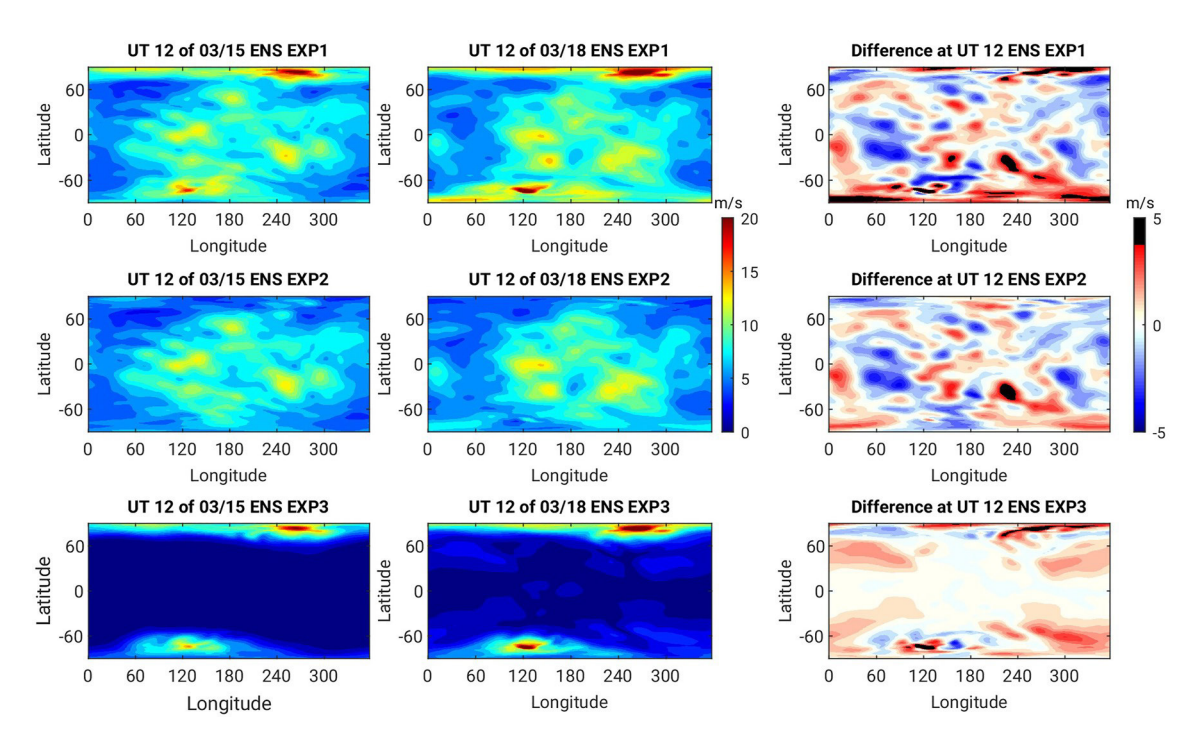


Figure 10. Longitude-latitude maps of the STDs of neutral zonal wind computed from WACCM-X ensembles at 4.687 × 10⁻⁸ hPa pressure level. From top to bottom are results from ENS EXP1, ENS EXP2, and ENS EXP3. The first and second columns are the standard deviation (STD) of the WACCM-X ensemble at 12:00 UT of 15 and 18 March, respectively. The third column is the difference between the STD at 12:00 UT of 15 and 18 March. The red scale in the third column's subplots means that the STD at 12:00 UT of March 18 is larger than that at 12:00 UT of 15 March; the blue scale means that the STD at 12:00 UT of 18 March is smaller than that at 12:00 UT of 15 March.

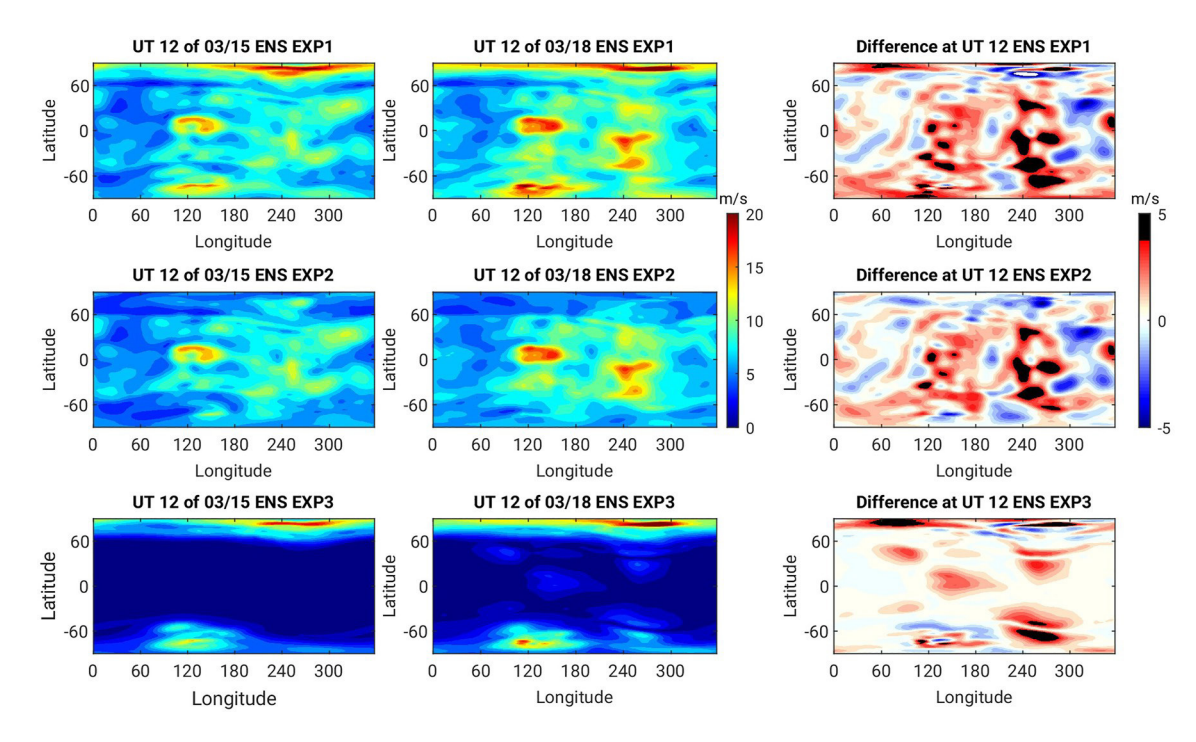


Figure 11. Longitude-latitude maps of the STDs of neutral meridional wind computed from model ensembles at 4.687×10^{-8} hPa pressure level. Similar to 10 but for neutral meridional wind.

HSU AND PEDATELLA 13 of 17

15427990, 2023, 4, Downloaded from https://agupubs.onlinelibrary.wiely.com/doi/10.1092/0223W003216, Wiley Online Library on [11/05/2023]. See the Terms and Conditions (https://onlinelibrary.viely.com/erms-and-conditions) on Wiley Online Library for rules of use; OA articles are governed by the applicable Cerative Commons

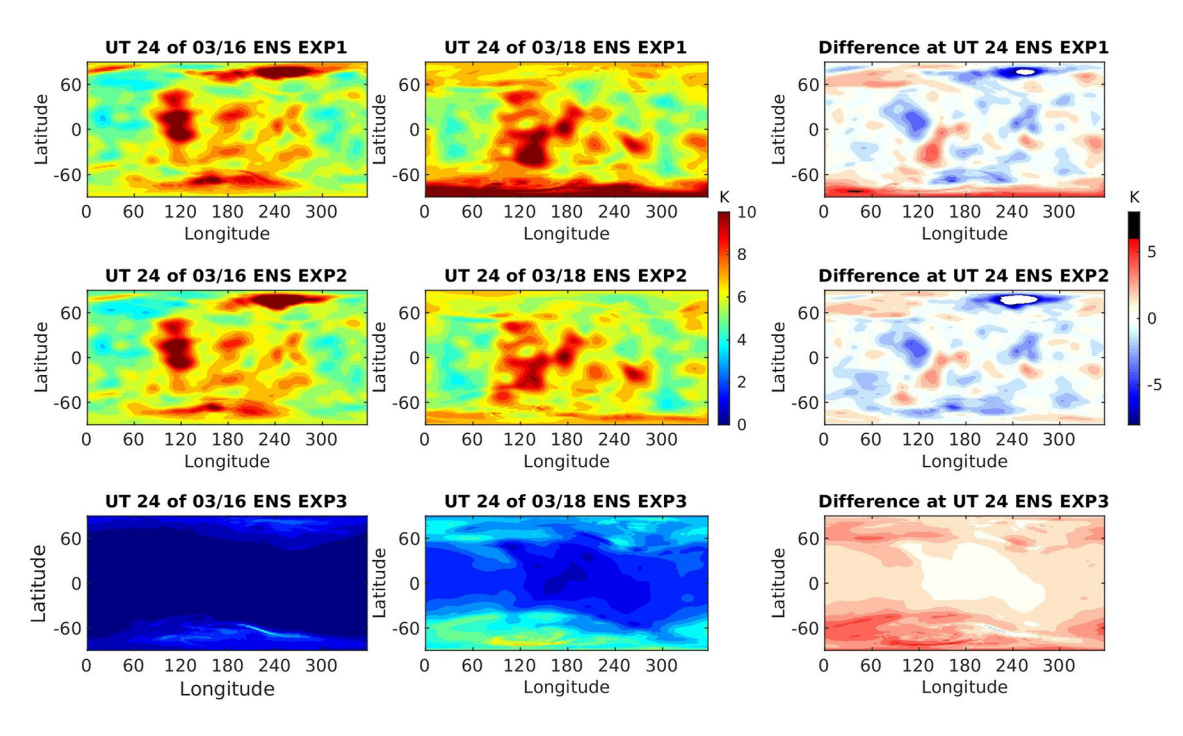


Figure 12. Longitude-latitude maps of the STDs of neutral temperature computed from model ensembles at 4.687×10^{-8} hPa pressure level. Similar to 10 but for neutral temperature.

4. Discussion

The atmosphere is chaotic by nature and this limits the predictability. In this study, Gaussian noise was added to the neutral zonal and meridional winds and temperature fields at the beginning of ENS EXP1 and ENS EXP2. The initial perturbation grows during the experiment period because of the internal model dynamics. Liu et al. (2009) explored the chaotic divergence of initial conditions and predictability using the WACCM.

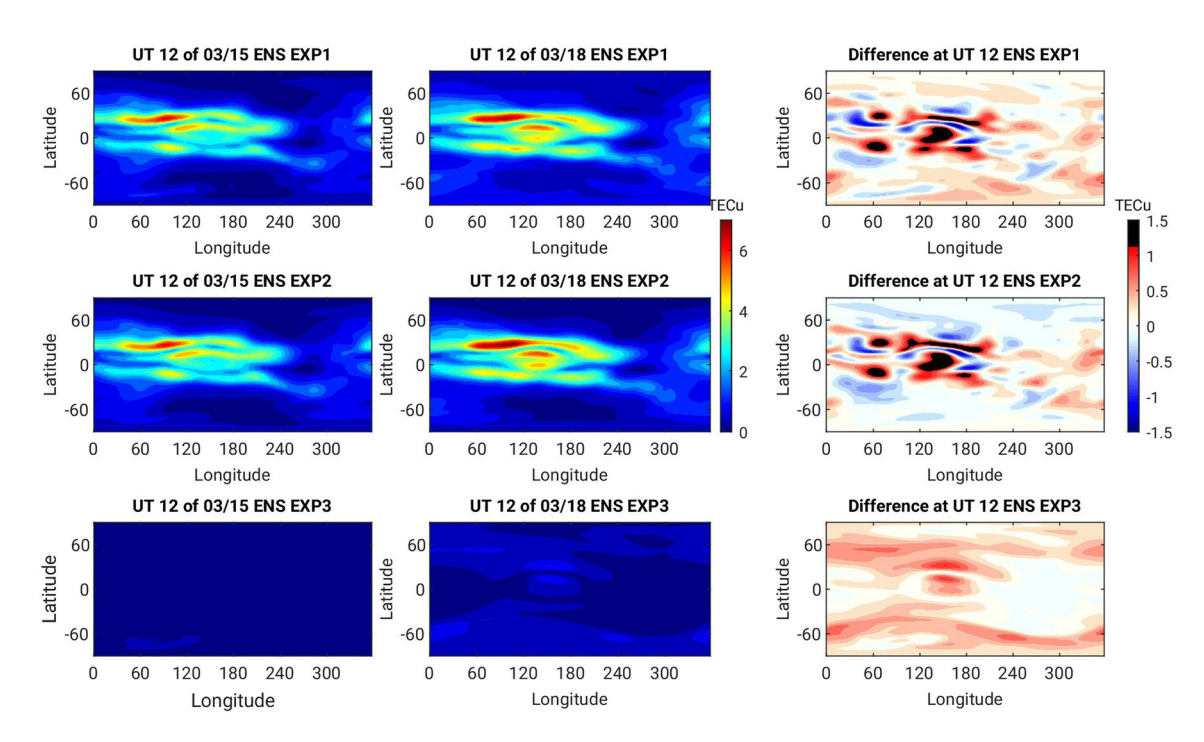


Figure 13. Longitude-latitude maps of the STDs of total electron content (TEC) computed from model ensembles. Similar to 10 but for TEC.

HSU AND PEDATELLA 14 of 17

15427390, 2023, 4, Downloaded from https://agupubs.onlinelibrary.wiley.com/doi/10.1029/2022SW003216, Wiley Online Library on [11/05/2023]. See the Terms and Conditions (https://agupubs.onlinelibrary.wiley.com/doi/10.1029/2022SW003216, Wiley Online Library on [11/05/2023]. See the Terms and Conditions (https://agupubs.onlinelibrary.wiley.com/doi/10.1029/2022SW003216, Wiley Online Library on [11/05/2023]. See the Terms and Conditions (https://agupubs.onlinelibrary.wiley.com/doi/10.1029/2022SW003216, Wiley.Com/doi/10.1029/2022SW003216, Wiley.Com/doi/10.1029/2022SW003

tions) on Wiley Online Library for rules of use; OA articles are governed by the applicable Creative Commons License

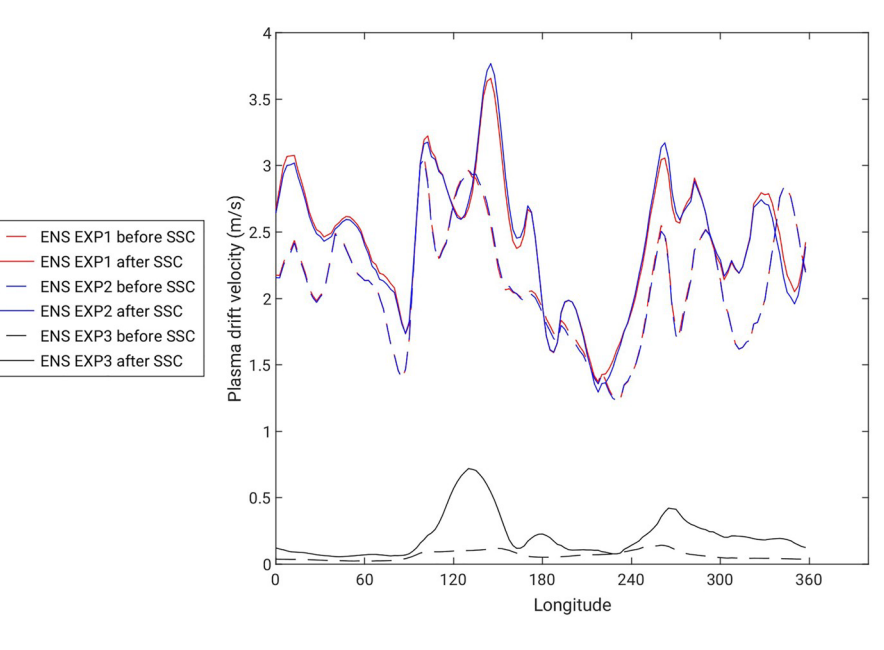


Figure 14. The STDs of vertical plasma drift along geomagnetic equator computed from model ensembles. Dash and solid lines are STDs at 12:00 UT of 15 and 18 March, respectively.

They perturbed the zonal mean temperature at 82°N and zonal mean zonal wind at 62°N and at both latitudes at 10 hPa to generate 10 WACCM ensemble members to investigate how the error grows in the model. The error growth in the middle and upper atmosphere is significantly reduced if the lower atmosphere is regularly reinitialized. Smith et al. (2017) investigated the dynamical influence of the lower and middle atmosphere on the upper mesosphere and lower thermosphere. They nudged the WACCM horizontal wind and temperature over part of the vertical range toward a true simulation. They found that the error growth largely depends on the vertical extent and frequency of the data used for nudging the model and the method used for representing gravity wave drag. Both of their study focus on understanding the mechanism behind the error growth and reducing it to improve the deterministic simulation result. In this study, we bring this issue to the probabilistic framework. Instead of reducing the error growth, we focus on characterizing how this uncertainty in the lower atmosphere forcing can influence the uncertainty in the ionosphere, while also considering the uncertainty in high-latitude forcing.

Pedatella et al. (2018) generate ensemble TIE-GCM simulation with perturbed electric potential and auroral energy flux. The STD used to perturb the electric potential was computed from typical values of observed high latitude electric field variability. In their study, the mean electric potential was in a range of ±50 keV, and the STD reached 30% of the mean, while in our ENS EXP3, the mean electric potential is in a range of ±30 keV and the STD is only 5% of the mean (shown in Figure S5 of Supporting Information S1). This indicates that only a small variation is shown in the upper atmosphere in ENS EXP3 compared with their study. However, the STD used in Pedatella et al. (2018) is constant over time and is not related to the analysis error of the AMIE. If the AMGeO and SuperDARN can provide more realistic estimates of the uncertainty, especially the uncertainty contributed from small-scale electric fields, only a small electric potential uncertainty that can vary under different geomagnetic conditions need to be considered. Pedatella and Liu (2018) perturb lower atmosphere in the WACCM-X with the same method as this study. The TEC changes between different ensemble members are up to 20% and 40% during quiet and storm times. The changes between different ensemble members in ENS EXP2 are up to about 50% during storm time (shown in Figure S6 of Supporting Information S1), which is comparable with the work of Pedatella and Liu (2018). Ensemble simulation experience 5 (TIE-GCM/ENS-5) in Hsu et al. (2021) perturb solar irradiance, high-latitude electric potential, auroral energy flux, and solar irradiance forcing the in the TIE-GCM during a minor storm period. The variance of equatorial vertical plasma drift during the storm period is about 15 m/s which is about 3.87 m/s in STD. This is larger than the result shown in this study, which might relate to the fact that the uncertainty of solar irradiance forcing is not being considered. A more comprehensive study that can take both the uncertainties of auroral energy flux forcing and solar irradiance into account.

HSU AND PEDATELLA 15 of 17

5. Conclusions

The purpose of the present study is to evaluate the sensitivity of thermospheric and ionospheric states to the uncertainties of the high-latitude electric potential and lower-atmospheric tide and wave forcings. The high-latitude electric potential forcing uncertainty and lower-atmospheric tide and wave forcing uncertainty are estimated in two ways. Analysis error covariance of the electric potential in an assimilative procedure of high-latitude electric potential, AMGeO, is used as the electric potential forcing uncertainty. This provides a data-based and time-varying electric potential forcing uncertainty. 40 high-latitude electric potential fields are sampled based on this uncertainty. On the other hand, the lower neutral atmosphere in a whole atmosphere model, WACCM-X, is perturbed to generate 40 lower atmospheric conditions through chaotic divergence. These 40 lower atmospheric conditions can lead to different internal tide and wave forcings. After that, 40 pairs of high-latitude electric potential fields and lower atmospheric conditions are applied to different WACCM-X ensemble members to drive ensemble simulation experiments. The spread of the neutral and ionized states from WACCM-X ensemble members can help estimate the sensitivity of the thermosphere and ionosphere to the uncertainties of forcings according to the Monte-Carlo algorithm. Three WACCM-X ensemble simulation experiments, ENS EXP1, ENS EXP2, and ENS EXP3, are launched with different combinations of forcing perturbations during the period of the 2013 St. Patrick's Day geomagnetic storm.

Although the impact of high-latitude electric potential uncertainty on low-latitude and quiet period thermospheric and ionospheric states is small, it is not negligible during the storm period. Uncertainties of lower atmospheric wave and tide forcings lead to a significant periodic variability of the uncertainties of upper atmosphere in the model, and is more important in low-latitude region than in the high-latitude region. The thermospheric and ionospheric states become even more sensitive if we take uncertainty of both forcings into account as show by ENS EXP1. STD is used to quantity the uncertainty of the thermosphere and ionosphere in different experiments. The STDs from the ENS EXP1, ENS EXP2, and ENS EXP3 don't have a clear linear relation, indicating that the impact of the uncertainties of high-latitude electric potential and lower-atmospheric waves and tides is not superposed linearly. By taking both the uncertainties of high-latitude electric potential and lower atmospheric wave and tide forcings into account the maximum STD of the temperature states at 4.687×10^{-8} hPa pressure level reaches 10.44 K, and that of the zonal and meridional winds reach 27.90 m/s and 32.75 m/s. For the ionized part, the maximum STD of the plasma drift and TEC calculated from WACCM-X ensemble reaches 0.14 m/s and 6.50 TECu. The typical thermosphere-ionosphere simulation result is based on given forcings which might include significant errors or bias in themselves. Therefore, the simulation result with this kind of deterministic way is likely to have significant error or bias that is difficult to insight. It is crucial to building up a comprehensive knowledge of the response of the model simulation to forcing uncertainties. The ensemble simulation experiments presented in this study provide a first insight of how significant the discrepancy of simulated thermospheric-ionospheric result may be caused by small error or bias in the high-latitude electric potential and lower atmospheric wave and tide forcing estimation. This study is also very useful for space weather prediction since background error estimation is an important set when doing data assimilation.

Data assimilation is a method that can calculate an analysis physical state by optimally combining the observed physical state with modeled physical state. The observation and background errors are two critical factors in determining the weight of the observed physical state and modeled physical state. Understanding the potential model error due to the forcing uncertainties helps improve the space weather data assimilation. We only present the sensitivity of a few key states to the uncertainties of the high-latitude electric potential and low-atmospheric wave and tide forcings during the period of the 2013 St. Patrick's Day geomagnetic storm. The uncertainties of more forcings, including the solar irradiance and energetic particle precipitation, need to be estimated and their impact on the model under different conditions need to be examined. For example, the uncertainties of energetic particle precipitation and its impact under different solar activity levels, or uncertainties of the solar irradiance and its impact during difference seasons. More studies of the relevant topic need to be carried out in the future to comprehensively understand the sensitivity of thermospheric and ionospheric model to the uncertainties of different forcings under different conditions.

Data Availability Statement

The WACCM-X + DART can be downloaded from the NCAR Data Assimilation Research Section website, https://www.image.ucar.edu/DAReS/DART/. The AMGeO can be obtained by request through the AMGeO website, https://amgeo.colorado.edu/. The major experiment result can be found on Open Science Framework, https://doi.org/10.17605/OSF.IO/GJZWT and https://doi.org/10.17605/OSF.IO/3MVQD.

HSU AND PEDATELLA 16 of 17

use; OA articles are governed by the applicable Creative Commons

Acknowledgments

This work was supported by the DARPA SEE program as part of the SEPHIR project. This material is based upon work supported by the National Center for Atmospheric Research (NCAR), which is a major facility sponsored by the National Science Foundation under Cooperative Agreement No. 185297. The authors acknowledge high-performance computing support from Cheyenne (https://doi. org/10.5065/D6RX99HX) provided by NCAR's Computational and Information Systems Laboratory, sponsored by the NSF. The authors also appreciate all valuable suggestions and help from the AMGeO Collaboration at the University of Colorado Boulder.

References

- AMGeO Collaboration. (2019). A Collaborative Data Science Platform for the Geospace Community: Assimilative Mapping of Geospace Observations (AMGeO) v1.0.0. [Computer software manual]. Zenodo. https://doi.org/10.5281/zenodo.3564914
- Chisham, G., Lester, M., Milan, S. E., Freeman, M. P., Bristow, W. A., Grocott, A., et al. (2007). A decade of the Super Dual Auroral Radar Network (SuperDARN): Scientific achievements, new techniques and future directions. *Surveys in Geophysics*, 28(1), 33–109. https://doi.org/10.1007/s10712-007-9017-8
- Cousins, E. D. P., Matsuo, T., & Richmond, A. D. (2013). SuperDARN assimilative mapping. *Journal of Geophysical Research: Space Physics*, 118(12), 7954–7962. https://doi.org/10.1002/2013|A019321
- Cousins, E. D. P., Matsuo, T., & Richmond, A. D. (2015). Mapping high-latitude ionospheric electrodynamics with SuperDARN and AMPERE. Journal of Geophysical Research: Space Physics, 120(7), 5854–5870. https://doi.org/10.1002/2014JA020463
- Cousins, E. D. P., & Shepherd, S. G. (2010). A dynamical model of high-latitude convection derived from SuperDARN plasma drift measurements. *Journal of Geophysical Research*, 115(A12). https://doi.org/10.1029/2010ja016017
- Emery, B. A., Roble, R. G., Ridley, E. C., Richmond, A. D., Knipp, D. J., Crowley, G., et al. (2012). Parameterization of the ion convection and the auroral oval in the near thermospheric general circulation models (Technical Report). National Center for Atmospheric Research.
- Gjerloev, J. W. (2009). A global ground-based magnetometer initiative. Eos, Transactions American Geophysical Union, 90(27), 230–231. https://doi.org/10.1029/2009E0270002
- Häusler, K., Hagan, M. E., Baumgaertner, A. J. G., Maute, A., Lu, G., Doornbos, E., et al. (2014). Improved short-term variability in the thermosphere-inosphere-mesosphere-electrodynamics general circulation model. *Journal of Geophysical Research: Space Physics, 119*(8), 6623–6630. https://doi.org/10.1002/2014JA020006
- Heelis, R. A., Lowell, J. K., & Spiro, R. W. (1982). A model of the high-latitude ionospheric convection pattern. *Journal of Geophysical Research*, 87(A8), 6339–6345. https://doi.org/10.1029/JA087iA08p06339
- Hsu, C.-T., Matsuo, T., Maute, A., Stoneback, R., & Lien, C.-P. (2021). Data-driven ensemble modeling of equatorial ionospheric electrodynamics: A case study during a minor storm period under solar minimum conditions. *Journal of Geophysical Research: Space Physics, 126*(2), e2020JA028539. https://doi.org/10.1029/2020JA028539
- Lee, I. T., Matsuo, T., Richmond, A. D., Liu, J. Y., Wang, W., Lin, C. H., et al. (2012). Assimilation of FORMOSAT-3/COSMIC electron density profiles into a coupled thermosphere/ionosphere model using ensemble Kalman filtering. *Journal of Geophysical Research*, 117(A10), A10318. https://doi.org/10.1029/2012|A017700
- Liu, H. L., Bardeen, C. G., Foster, B. T., Lauritzen, P., Liu, J., Lu, G., et al. (2018). Development and validation of the Whole Atmosphere Community Climate Model with thermosphere and ionosphere extension (WACCM-X 2.0). *Journal of Advances in Modeling Earth Systems*, 10(2), 381–402. https://doi.org/10.1002/2017MS001232
- Liu, H.-L., Sassi, F., & Garcia, R. R. (2009). Error growth in a whole atmosphere climate model. *Journal of the Atmospheric Sciences*, 66(1), 173–186. https://doi.org/10.1175/2008JAS2825.1
- Marsh, D. R., Mills, M. J., Kinnison, D. E., Lamarque, J.-F., Calvo, N., & Polvani, L. M. (2013). Climate change from 1850 to 2005 simulated in CESM1 (WACCM). *Journal of Climate*, 26(19), 7372–7391. https://doi.org/10.1175/JCLI-D-12-00558.1
- Matsuo, T. (2020). Recent progress on inverse and data assimilation procedure for high-latitude ionospheric electrodynamics. In M. Dunlop & H. Lühr (Eds.), *Ionospheric multi-spacecraft analysis tools* (Vol. 17, pp. 219–232). Springer. https://doi.org/10.1007/978-3-030-26732-2_10
- Matsuo, T., Richmond, A. D., & Lu, G. (2005). Optimal interpolation analysis of high-latitude ionospheric electrodynamics using empirical orthogonal functions: Estimation of dominant modes of variability and temporal scales of large-scale electric fields. *Journal of Geophysical Research*, 110(A6), A06301. https://doi.org/10.1029/2004JA010531
- Neale, R. B., Richter, J., Park, S., Lauritzen, P. H., Vavrus, S. J., Rasch, P. J., & Zhang, M. (2013). The mean climate of the Community Atmosphere Model (CAM4) in forced SST and fully coupled experiments. *Journal of Climate*, 26(14), 5150–5168. https://doi.org/10.1175/ICLI-D-12-00236.1
- Newell, P. T., Sotirelis, T., & Wing, S. (2009). Diffuse, monoenergetic, and broadband aurora: The global precipitation budget. *Journal of Geophysical Research*, 114(A9), A09207. https://doi.org/10.1029/2009JA014326
- Newell, P. T., Sotirelis, T., & Wing, S. (2010). Seasonal variations in diffuse, monoenergetic, and broadband aurora. *Journal of Geophysical Research*, 115(A3), A03216. https://doi.org/10.1029/2009|A014805
- Pedatella, N. M., & Liu, H.-L. (2018). The influence of internal atmospheric variability on the ionosphere response to a geomagnetic storm. Geophysical Research Letters, 45(10), 4578–4585. https://doi.org/10.1029/2018GL077867
- Pedatella, N. M., Lu, G., & Richmond, A. D. (2018). Effects of high-latitude forcing uncertainty on the low-latitude and midlatitude ionosphere. Journal of Geophysical Research: Space Physics, 123(1), 862–882. https://doi.org/10.1002/2017JA024683
- Qian, L., Burns, A. G., Emery, B. A., Foster, B., Lu, G., Maute, A., et al. (2014). The NCAR TIE-GCM. In J. Huba, R. Schunk, & G. Khazanov (Eds.), Modeling the ionosphere–thermosphere system (pp. 73–83). American Geophysical Union (AGU). https://doi.org/10.1002/9781118704417.ch7 Richmond, A. D. (1992). Assimilative mapping of ionospheric electrodynamics. Advances in Space Research, 12(6), 59–68. https://doi.org/10.1016/0273-1177(92)90040-5
- Richmond, A. D., & Kamide, Y. (1988). Mapping electrodynamic features of the high-latitude ionosphere from localized observations: Technique. *Journal of Geophysical Research*, 93(A6), 5741–5759. https://doi.org/10.1029/JA093iA06p05741
- Richmond, A. D., Ridley, E. C., & Roble, R. G. (1992). A thermosphere/ionosphere general circulation model with coupled electrodynamics. *Geophysical Research Letters*, 19(6), 601–604. https://doi.org/10.1029/92GL00401
- Rienecker, M. M., Suarez, M. J., Gelaro, R., Todling, R., Bacmeister, J., Liu, E., et al. (2011). MERRA: NASA's modern-era retrospective analysis for research and applications. *Journal of Climate*, 24(14), 3624–3648. https://doi.org/10.1175/JCLI-D-11-00015.1
- Robinson, R. M., Vondrak, R. R., Miller, K., Dabbs, T., & Hardy, D. (1987). On calculating ionospheric conductances from the flux and energy of precipitating electrons. *Journal of Geophysical Research*, 92(A3), 2565–2569. https://doi.org/10.1029/JA092iA03p02565
- Smith, A. K., Pedatella, N. M., Marsh, D. R., & Matsuo, T. (2017). On the dynamical control of the mesosphere-lower thermosphere by the lower and middle atmosphere. *Journal of the Atmospheric Sciences*, 74(3), 933–947. https://doi.org/10.1175/JAS-D-16-0226.1
- Weimer, D. R. (2005). Improved ionospheric electrodynamic models and application to calculating Joule heating rates. *Journal of Geophysical Research*, 110(A5), A05306. https://doi.org/10.1029/2004JA010884

HSU AND PEDATELLA 17 of 17